UVIT Study of the MAgellanic Clouds (U-SMAC). II. A Far-UV Catalog of the Small Magellanic Cloud: Morphology and Kinematics of Young Stellar Population

Sipra Hota[1,2] ⓘ, Annapurni Subramaniam[1] ⓘ, Prasanta K. Nayak[3] ⓘ, and Smitha Subramanian[1] ⓘ

[1] Indian Institute of Astrophysics, 2nd Block, Koramangala, Bangalore-560034, India
[2] Pondicherry University, R.V. Nagar, Kalapet, Puducherry-605014, India
[3] Institute of Astrophysics, Pontificia Universidad Católica de Chile, Av. Vicuña MacKenna 4860, Santiago 7820436, Chile

Abstract

The Small Magellanic Cloud (SMC) is an irregular dwarf galaxy that has recently undergone an interaction with the Large Magellanic Cloud. The young massive stars in the SMC formed in the disturbed low-metallicity environment are important targets in astrophysics. We present a catalog of ∼76,800 far-ultraviolet (FUV) sources toward the SMC detected using the Ultra Violet Imaging Telescope onboard AstroSat. We created an FUV catalog with ∼62,900 probable SMC members which predominantly comprise main-sequence, giant, and subgiant stars. We selected four young populations (Young 1, Young 2, Young 3, and Blue Loop (BL) stars) identified from the Gaia optical color–magnitude diagram to study the morphology and kinematics of the young SMC using this catalog. We detect a clumpy morphology with a broken bar, a shell-like structure, and the inner SMC Wing for the four stellar populations. The eastern region and the northeastern regions are mainly populated by Young 1, 2, and 3 stars. The central region predominantly has the Young 2 and 3 populations, whereas the SW has BL stars, and Young 2 and 3 stars. The 2D kinematic study using proper motion (PM) reveals that Young 2 and 3 populations show two kinematically distinct subpopulations with low and high PM dispersion, whereas the Young 1 and BL stars show two kinematically distinct populations with low dispersion. Our analysis points to a kinematic disturbance along the R.A. direction for stars younger than ∼150 Myr located in the eastern region, with no significant disturbance along the decl.

Unified Astronomy Thesaurus concepts: Magellanic Clouds (990); Galaxy photometry (611); Ultraviolet astronomy (1736); Galaxy evolution (594)

Materials only available in the online version of record: *machine-readable table*

1. Introduction

The Large Magellanic Cloud (LMC) and the Small Magellanic Cloud (SMC) are the closest interacting galaxies to the Milky Way (MW), at a distance of ∼50 kpc (R. de Grijs et al. 2014; G. Pietrzyński et al. 2019) and ∼60 kpc (R. de Grijs & G. Bono 2015; D. Graczyk et al. 2020), respectively. Both the Clouds, the Magellanic Bridge, the Magellanic Stream, and the Leading Arm are together known as the Magellanic System. The Magellanic Bridge, which connects the LMC and the SMC, is composed of gas and stars, and its origin is due to the recent collision between the two galaxies at ∼200 Myr (J. V. Hindman et al. 1963; M. J. Irwin et al. 1985; L. T. Gardiner et al. 1994; E. Muller & K. Bekki 2007; P. Zivick et al. 2019). The Magellanic Stream (Y.-Z. Liu 1992; L. T. Gardiner et al. 1994) is a gaseous tail behind the Clouds, orbiting the MW, and the counterpart of the Stream, known as the Leading Arm (first detected by M. E. Putman et al. 1998), is approaching the Galactic disk (S. Lucchini et al. 2020). Both the Stream and the Leading Arm are tidal features that formed due to MW–LMC–SMC interactions (Y.-Z. Liu 1992; L. T. Gardiner et al. 1994; D. L. Nidever et al. 2008, 2010; E. D'Onghia & A. J. Fox 2016; S. Lucchini et al. 2020). The LMC and the SMC have undergone repeated interactions between each other (K. Glatt et al. 2010; G. Indu &

A. Subramaniam 2011; P. K. Nayak et al. 2018; S. Rubele et al. 2018; Y. C. Joshi & A. Panchal 2019) and they are in their first infall toward the MW (N. Kallivayalil et al. 2006; G. Besla et al. 2007; V. Chandra et al. 2023). However, E. Vasiliev (2023) suggested the second passage of the LMC around the MW.

The SMC is a gas-rich irregular dwarf galaxy with a less pronounced bar and an eastern extension, known as the SMC Wing (G. de Vaucouleurs & K. C. Freeman 1972; S. Subramanian & A. Subramaniam 2012; V. Ripepi et al. 2017; D. El Youssoufi et al. 2019). The SMC is nearly ten and hundred times less massive (dynamical mass $\approx 10^9 M_\odot$) than the LMC and the MW, respectively (S. Stanimirović et al. 2004; R. P. van der Marel et al. 2008; R. P. van der Marel & N. Kallivayalil 2014). Therefore, the morphology, dynamics, and evolution of the SMC have been significantly shaped by the gravitational interactions with both the LMC and the MW (M. E. Putman et al. 1998; P. Massana et al. 2020; B. L. Tatton et al. 2021). Different stellar populations of the SMC show distinct morphology (e.g., L. T. Gardiner & D. Hatzidimitriou 1992; C. Bot et al. 2004; D. El Youssoufi et al. 2019; Gaia Collaboration et al. et al. 2021a). The young population in the SMC is unevenly distributed, with a higher concentration in the central region and the SMC Wing that connects to the Magellanic Bridge (D. Zaritsky et al. 2000; S. Rubele et al. 2015; D. El Youssoufi et al. 2019). In the case of the older stellar population, their spatial distribution appears more uniform and spheroidal/ellipsoidal (e.g., D. Zaritsky et al. 2000; J. Harris & D. Zaritsky 2004; S. Stanimirović et al. 2004;

R. Haschke et al. 2012; S. Rubele et al. 2015; D. El Youssoufi et al. 2019). Studies have found that the SMC is elongated along the northeast-southwest (NE–SW) axis and NE of the SMC is closer to us (S. Subramanian & A. Subramaniam 2012; V. Scowcroft et al. 2016; V. Ripepi et al. 2017; C. E. Murray et al. 2024).

The SMC outskirts are home to several stellar substructures (A. Pieres et al. 2017; D. Mackey et al. 2018; V. A. Belokurov & D. Erkal 2019; P. Massana et al. 2020), such as northeastern SMC shell (younger than 500 Myr; D. Martínez-Delgado et al. 2019; S. Hota et al. 2024; J. D. Sakowska et al. 2024), the existence of the tidal counterpart of the Magellanic Bridge (Counter Bridge; B. Dias et al. 2021), the West Halo, and a structure moving away from the SMC as confirmed in the western outskirts of the SMC (B. Dias et al. 2016; F. Nieder-hofer et al. 2018; P. Zivick et al. 2018; B. Dias et al. 2022). L. R. Cullinane et al. (2023) identified two different populations in the extreme south of the SMC outskirts. One population exhibits the properties of the SMC outskirts, while the other is the debris from the SMC that was tidally stripped due to interaction with the LMC. A. O. Omkumar et al. (2021) found a foreground stellar population in the eastern SMC outskirts, which they linked to the counterpart of the gaseous Magellanic Bridge.

Observing the SMC across various wave bands is essential to trace its morphology as a function of the stellar population, which is a proxy to probe the evolution of the SMC. Near-infrared (NIR) observations of the SMC were conducted by the Two Micron All Sky Survey (2MASS; M. Cohen et al. 2003) and by Visible and Infrared Survey Telescope for Astronomy (VISTA) survey of the Magellanic Clouds system (VMC; M. R. L. Cioni et al. 2011). Medium and far-infrared (FIR) surveys were carried out by Spitzer (K. D. Gordon et al. 2011). Gaia has provided optical photometry and astrometry observations of the SMC (Gaia Collaboration et al. et al. 2016, 2021a, 2021b; Gaia Collaboration et al. 2023) and the Survey of the MAgellanic Stellar History has supplied deep optical data of the SMC (SMASH; D. L. Nidever et al. 2017, 2021). To understand the recent interaction and its influence on the spatial distribution of the young population, the far-ultraviolet (FUV) band is essential because it is a significant tracer of young stars that exhibit a peak in their flux in the FUV wave band (R. H. Cornett et al. 1997; A. Devaraj et al. 2023; S. Hota et al. 2024). The Hubble Space Telescope (HST) provides high resolution images in multiple passbands, including the FUV, but the coverage is limited due to a small field of view (FOV). Other instruments, such as the Ultraviolet Imaging Telescope (UIT; R. H. Cornett et al. 1994, 1997) and Swift/UVOT (UltraViolet and Optical Telescope; N. Gehrels et al. 2004) with spatial resolution greater than $2''$ have also observed the SMC. The SMC was partially observed by the Galaxy Evolution Explorer (GALEX; R. Simons et al. 2014) in the near-ultraviolet (NUV) and FUV bands with a spatial resolution of $\sim 5''$. However, some areas of the SMC lack FUV observations by GALEX. The Ultra Violet Imaging Telescope (UVIT; S. N. Tandon et al. 2017a) with its superior spatial resolution ($\sim 1{.}''4$) to GALEX, UIT, and UVOT is capable of providing a good FUV coverage of the SMC, which has been lacking so far.

In this work, we present a point source catalog of the SMC in the FUV band based on the UVIT images of 39 fields in the SMC. The catalog is cross-matched with the VMC and Gaia Data Release 3 (DR3; Gaia Collaboration et al. 2023) catalogs to provide the corresponding IDs. We also present the morphology and kinematics of various populations of the SMC that are detected in the FUV. This paper is arranged as follows. Section 2 covers the data used in this work and their analysis. We show the location of different types of populations on the color–magnitude diagrams (CMDs; UV–optical and IR CMDs) in Section 3. Sections 4 and 5 explore their morphology and kinematics, respectively. The discussion can be found in Section 6, and the summary and conclusions are given in Section 7.

2. Data and Analysis

2.1. Observation and Data Reduction

UVIT comprises two distinct telescopes of 38 cm in diameter; one is dedicated to the FUV (130–180 nm) channel, while the other one is for NUV (200–300 nm) and visible (VIS: 350–550 nm) channels. In each of these channels, multiple filters are also present (S. N. Tandon et al. 2020). The VIS observations are used primarily for drift correction due to the spacecraft's motion (S. N. Tandon et al. 2017a). UVIT has a field of view of $\sim 28'$ with a spatial resolution of $\sim 1{.}''4$. The comprehensive information regarding the instrument and calibration of UVIT are available in J. Postma et al. (2011), A. Kumar et al. (2012), A. Subramaniam et al. (2016a), and S. N. Tandon et al. (2017b). In this work, we utilized FUV images of 39 UVIT pointings in the medium passband filter; F172M (silica: 1717 ± 125 Å; S. N. Tandon et al. 2020). The Level 1 (L1) data for the UVIT observed fields are publicly available.[4] The 39 SMC fields used in this study are shown in Figure 1, where pointings are overlaid on the GALEX image, with each circle having the UVIT field of view. The observational details of the SMC fields are provided in Table 1. We note from Table 1 that out of 39 SMC fields, 25 SMC fields have exposure time >900 s, nine fields have exposure time between 400 and 830 s, while three fields have exposure time between 300 and 400 s. Two SMC fields, SMC-02 and SMC-42, exhibit shorter exposure time (<200 s). SMC-02 is situated on the periphery of the SMC's main body, whereas SMC-42 is located within the inner region of the SMC Wing. We note that this study does not include the regions of the SMC covered by S. Hota et al. (2024) and A. Devaraj et al. (2023).

The science-ready images of the SMC fields are created by processing the L1 data obtained by UVIT using the CCDLAB pipeline as described in J. E. Postma & D. Leahy (2017, 2021). This pipeline autonomously applies corrections such as flat-fielding, fixed pattern noise, and spacecraft drift. Astrometry of these science-ready images is done using the same pipeline with World Coordinate System (WCS) reference from Gaia DR3 data (Gaia Collaboration et al. 2023). Consequently, we obtain science-ready images accompanied by astrometry information of the SMC fields.

2.2. PSF Photometry

To determine the magnitudes of individual sources in the science-ready images of the SMC fields, we performed point-spread function (PSF) photometry. The PSF photometry involves the following major steps: detecting sources,

---

[4] https://astrobrowse.issdc.gov.in/astro_archive/archive/Home.jsp
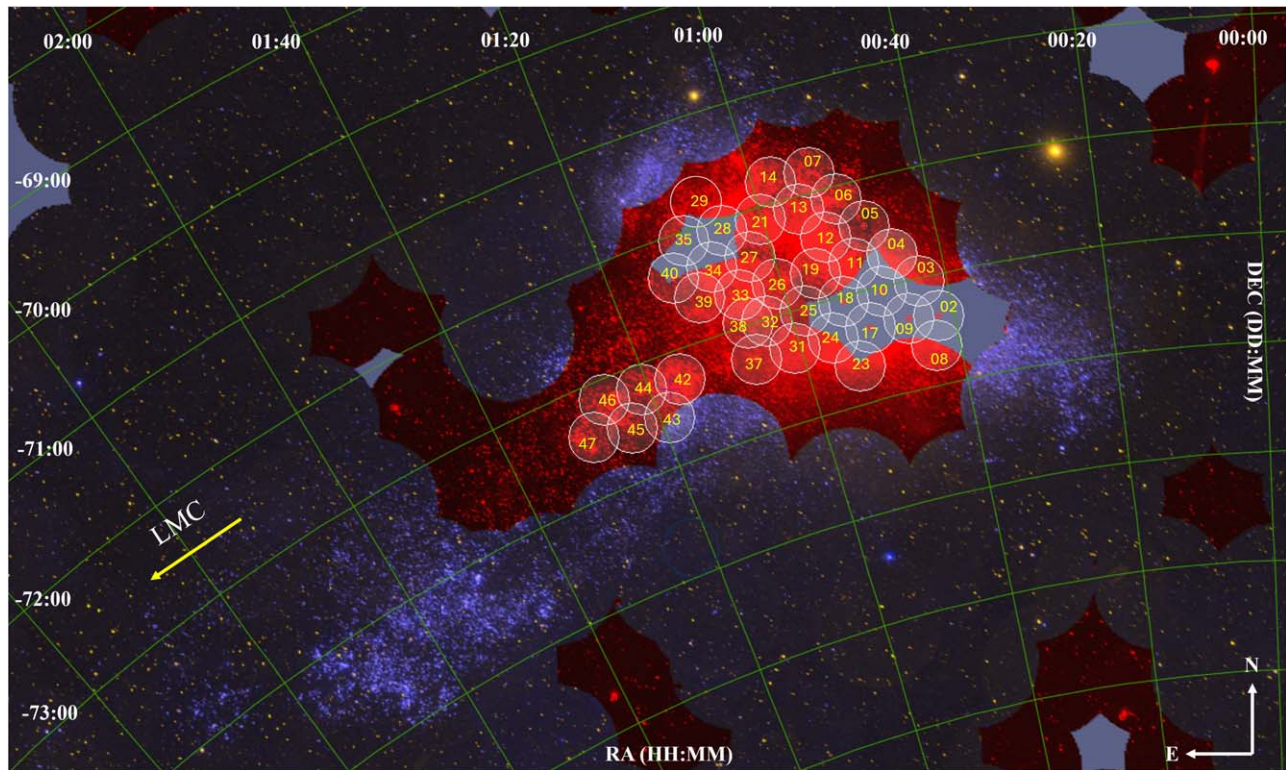
Figure 1. The SMC: UVIT observed fields in white circles are displayed over the GALEX background. The background is a two-color combined image of GALEX, where the blue color represents FUV observations, whereas the red color denotes NUV observations (encompassing both GR6 and GR7 data releases). The yellow arrow points in the direction of the LMC (V. Belokurov et al. 2017; M. De Leo et al. 2020).

performing aperture photometry, creating a model PSF, and applying the model PSF to all the detected sources. We conducted PSF photometry using the DAOPHOT package of the Image Reduction and Analysis Facility (IRAF; P. B. Stetson 1987) tool. First, we used the IMEXAM routine to estimate the background noise (sigma) and the full-width half-maxima (FWHM) of the sources in the image. Subsequently, the DAOFIND task is utilized for source detection, employing a threshold set at five times the background level. During this process, main parameters such as the exposure time of the observed field, the estimated FWHM of the sources, and the zero-point of the filter are imposed. Following that, aperture photometry was carried out using the PHOT task and a set of isolated bright stars was chosen to construct a model PSF using the PSF SELECT task. The PSF model was created by running the PSF task in IRAF and subsequently applied to all detected stars to determine the PSF magnitude simultaneously through the ALLSTAR task. PSF correction was performed to convert PSF magnitude to aperture magnitude. Afterwards, an aperture correction was applied to all detected sources using the curve of growth for a few isolated bright stars in the images. We transformed the instrumental magnitude to the AB magnitude scale using the relation (S. N. Tandon et al. 2017a),

$$m_{AB} = -2.5\log(CPS) + ZP \tag{1}$$

where CPS is the counts per second, and ZP is the zero-point given by

$$ZP = (-2.5\log(UC) \cdot (\lambda_{mean})^2) - 2.407. \tag{2}$$

The zero-point value of the F172M filter is 16.274, as specified in S. N. Tandon et al. (2020). Saturation correction was applied for all the detected sources, as detailed in

S. N. Tandon et al. (2017b). The variation of PSF fit error with the obtained FUV magnitude and exposure time is shown in Figure 2 using seven sample SMC fields: SMC-42 (187.8 s), SMC-39 (395.4 s), SMC-46 (472.0 s), SMC-26 (634.3 s), SMC-33 (825.8 s), SMC-10 (954.8 s), and SMC-17 (1022.3 s). Other observed fields of the SMC exhibit a similar trend. To avoid the edge effect, sources within a ~1′ annulus near the edges of the observed fields are excluded.

2.3. Completeness Factor

The peak of the magnitude distribution of an observed field is a pointer to the completeness in the data (D. A. Leahy et al. 2020; A. Devaraj et al. 2023). In Figure 3(a), we have shown the distribution of FUV magnitude of SMC fields with seven different exposure times (same as in Figure 2). The distribution shows peaks in magnitudes between 17.5 and 19.5 mag, and we note a sudden drop in the number of fainter stars along with an increase in the FUV magnitude error, as shown in Figure 2. This points to a range in incompleteness in the observed fields that need to be quantified.

In order to quantitatively estimate the incompleteness in the data across the observed fields, we conducted artificial star tests (ASTs) on the above mentioned seven fields to determine the completeness factor (CF). We performed the AST using the DAOPHOT routine in IRAF. We randomly added artificial stars ranging between ~10% and 15% of the detected stars in the individual images. More details of the AST and CF can be found in R. Sagar & T. Richtler (1991), Y. Hu et al. (2011), S. Sahu et al. (2022). Then, we followed the same procedure for the PSF photometry as in Section 2.2 and recovered the

Observed Field	R.A. (deg)	Decl. (deg)	t_{exp} (s)
SMC-02	10.47	−73.38	153.0
SMC-03	10.84	−73.03	954.2
SMC-04	11.49	−72.73	953.9
SMC-05	12.11	−72.43	954.9
SMC-06	12.72	−72.13	445.3
SMC-07	13.30	−71.82	955.1
SMC-08	10.76	−73.64	954.6
SMC-09	11.43	−73.34	954.3
SMC-10	12.08	−73.04	954.8
SMC-11	12.70	−72.74	954.9
SMC-12	13.31	−72.43	954.4
SMC-13	13.90	−72.13	951.6
SMC-14	14.46	−71.82	951.7
SMC-17	12.69	−73.35	1022.3
SMC-18	13.32	−73.04	965.3
SMC-19	13.92	−72.74	957.2
SMC-21	15.07	−72.12	955.8
SMC-23	13.32	−73.65	952.7
SMC-24	13.95	−73.35	951.0
SMC-25	14.55	−73.04	952.6
SMC-26	15.14	−72.73	634.3
SMC-27	15.70	−72.42	952.0
SMC-28	16.24	−72.10	953.7
SMC-29	16.77	−71.79	953.9
SMC-31	15.21	−73.34	951.3
SMC-32	15.79	−73.03	951.3
SMC-33	16.35	−72.71	825.8
SMC-34	16.89	−72.40	472.0
SMC-35	17.42	−72.08	485.3
SMC-37	16.46	−73.32	377.0
SMC-38	16.37	−72.98	371.0
SMC-39	17.54	−72.62	395.4
SMC-40	18.08	−72.37	471.8
SMC-42	18.97	−73.27	187.8
SMC-43	19.71	−73.55	951.7
SMC-44	20.21	−73.23	951.6
SMC-45	20.97	−73.51	470.6
SMC-46	21.45	−73.18	472.0
SMC-47	22.23	−73.46	471.5

Note. R.A. and decl. are the central coordinates of the observed fields.

added stars. The CF is estimated as the ratio of the number of recovered stars to the number of added stars.

We executed AST twice for the magnitude range of 12–21 mag and thrice for 15–21 mag, 18–21 mag, 19–21 mag, and 20–21 mag on an image. Then, the average CF is estimated from the multiple ASTs for a field and the percentage of completeness is estimated. The same procedure of AST is followed for all the images. Figure 3(b) shows the variation of completeness fraction with the FUV magnitude for seven SMC fields. Extending these CFs to all fields, we conclude that the observed fields exhibit 100% completeness at ∼16 mag, beyond which the completeness starts to reduce. For artificial stars up to 18 mag, all considered images (with different exposures and crowding) show a recovery rate of around 90%. Therefore, we consider a completeness of 90% or more at ∼18 mag (FUV) for all the observed SMC fields.

2.4. FUV Catalog and Cross-matching

To produce the FUV catalog, we combined the photometric data of all the 39 UVIT observed fields. The presence of data

duplication in the overlapping regions is addressed by considering the source with better signal-to-noise ratio and/or photometric error. For the catalog, we selected FUV sources with a magnitude error of ⩽0.2 mag (for signal-to-noise ratio; S/N ⩾5) and an FUV magnitude > 13.2 mag because the FUV sources brighter than ∼13.2 mag may be saturated (S. N. Tandon et al. 2017b). With the above criteria, a catalog with ∼76,800 FUV sources is listed in Table 2. Though this catalog covers the inner SMC, we point out the presence of a gap in the observed area, centered around the coordinates (α, δ):(14°, −72°.5) as shown in Figure 1.

To better characterize the detected FUV sources in the SMC, we cross-matched these FUV sources with IR and optical data. We obtained the Gaia DR3 data (Gaia Collaboration et al. 2023) of the SMC with ADQL query in the Gaia archive[5] as mentioned in Gaia Collaboration et al. (2021a). The number of cross-matched UVIT-Gaia sources within a search radius of 1″ is 73,395 and their corresponding Gaia_DR3_Source_IDs are listed in the seventh column of Table 2. The PSF photometry catalog of the SMC in IR band (S. Rubele et al. 2018) as part of the VMC from the European Southern Observatory (ESO) archive[6] is cross-matched with the detected FUV sources within a search radius of 1″ to obtain 72,790 UVIT-VMC cross-matched sources (VMC_PSF_Source_ID is listed in 6th column of Table 2). We note that ∼70,900 FUV sources have both optical (Gaia) and IR (VMC) data, while ∼1450 FUV sources do not have either Gaia or VMC cross-matches.

We performed a cross-match of the FUV catalog (see Table 2) with the SIMBAD database using a search radius of 1″. This analysis revealed that 9133 stars were matched with the SIMBAD database, and we note that ∼30% of cross-matched sources are eclipsing binaries, and another ∼30% are classified as "star" (no spectral classification). We also found some UVIT-SIMBAD stars are classified as supergiants (∼200), white dwarfs (∼200), Be stars (∼650), and high-mass X-ray binaries (∼100). We also cross-matched our catalog with the catalog of 5324 massive stars in the SMC by A. Z. Bonanos et al. (2010), using a search radius of 1″ (UVIT observed fields cover only 65% of the catalog), and 2388 stars were identified. The majority of these cross-matched stars are of OB type (O-type: ∼132, B-type: ∼2000).

2.5. Most Probable FUV Sources of the SMC

To find the most probable FUV sources in the SMC, we considered only those FUV sources, that have Gaia counterparts. The spherical coordinates of the SMC are projected onto the XY-plane using the zenithal equidistant projection method, where we followed the X and Y conversion as defined in R. P. van der Marel & M.-R. L. Cioni (2001). For this, we considered the optical center of the SMC at $\alpha_{SMC} = 00^h 52^m 12^s.5$ and $\delta_{SMC} = −72° 49′ 43″$ (J2000; G. de Vaucouleurs & K. C. Freeman 1972). Here, we followed two criteria for selecting the most probable SMC sources. (1) We implemented a 3σ cutoff around the mean value of the parallax (Plx = 0.014 mas) and proper motion (PM) in both R.A. and decl. ($\mu_\alpha \cos \delta = 0.74$ mas yr^{-1}, $\mu_\delta = −1.25$ mas yr^{-1}) for the detected FUV sources. The resulting number of the most probable FUV sources of the SMC is 69,389. Still, there is a possibility that these FUV sources may be contaminated with
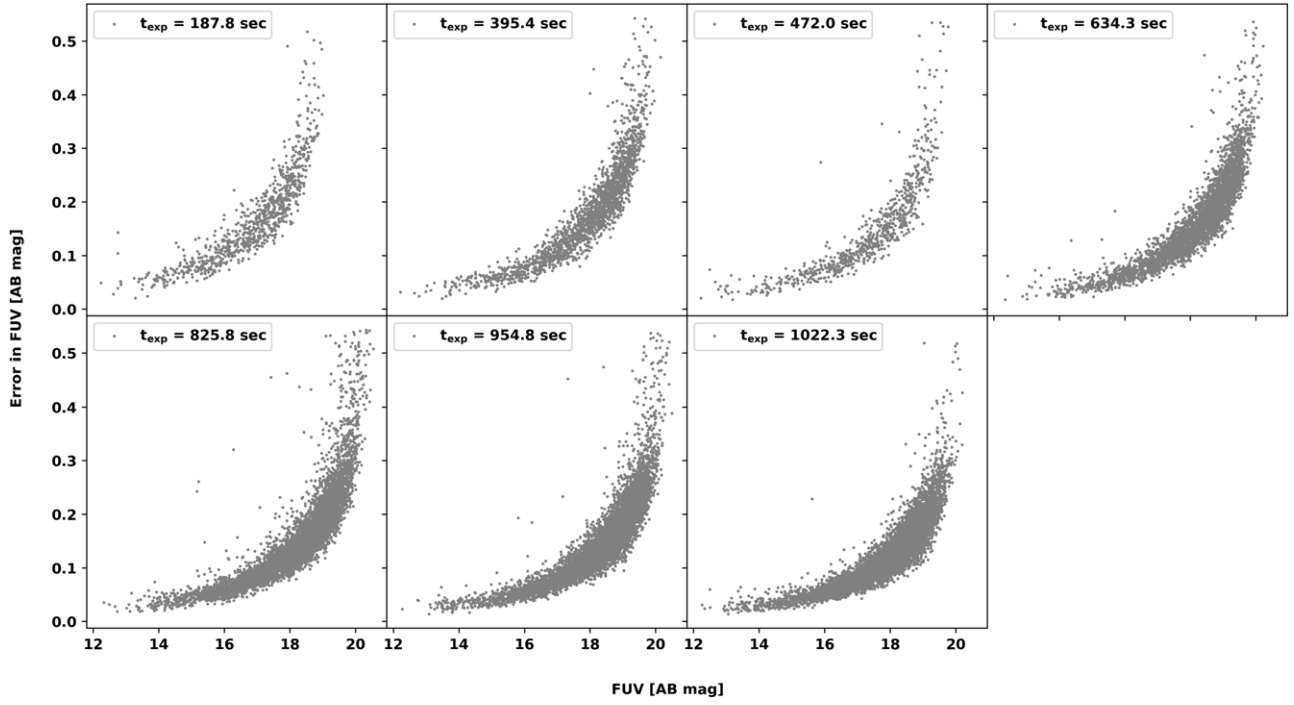
---

5   https://gea.esac.esa.int/archive/
6   https://archive.eso.org/cms/html

Figure 2. FUV magnitude vs. error in magnitude (PSF fit error) for various fields of the SMC with different exposure times.
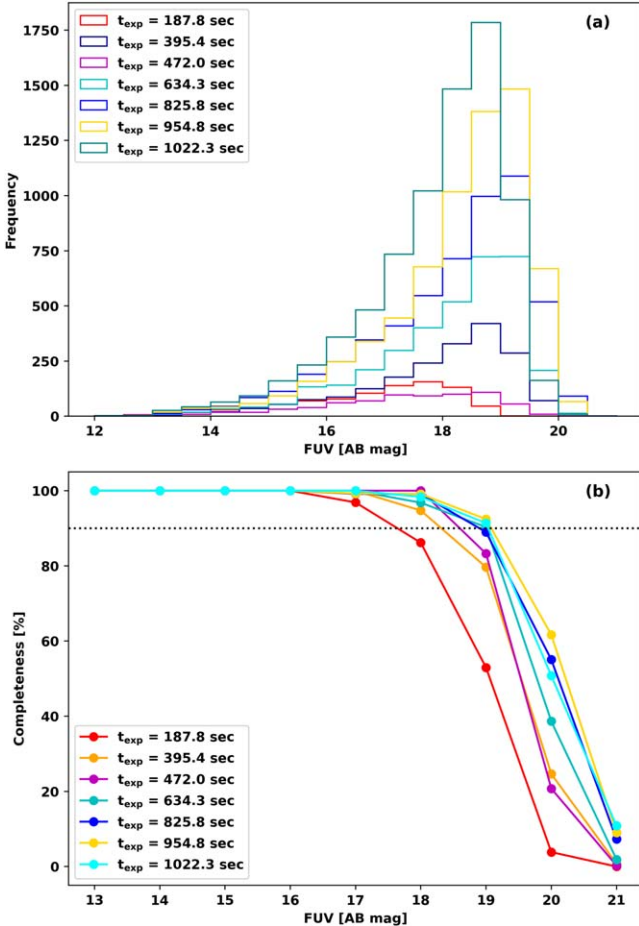

Figure 3. (a) The FUV magnitude distribution and (b) completeness in percentage for seven UVIT observed SMC fields with different exposure times. The black-dotted line represents 90% of completeness.

the background galaxies. (2) We cross-matched the FUV sources with the Gaia probability catalog of the SMC sources provided by Ó. Jiménez-Arranz et al. (2023). They obtained three samples of the SMC based on probability (P_{cut}) and G mag cutoff. We followed the same cut-offs to obtain three samples of the most probable SMC stars: (i) NN complete ($P_{cut} = 0.01$): 70,319 FUV sources, (ii) NN optimal ($P_{cut} = 0.31$): 68,621 FUV sources, and (iii) NN truncated-optimal sample ($P_{cut} = 0.31$ and $G < 19.5$ mag): 68,540 FUV sources (see Table 3). The spatial distribution of the SMC and MW sources, obtained from different methods, are shown in Figure 4(a). We note that the MW FUV stars show a similar spatial distribution as the SMC.

There is a possibility that Gaia sources are nonsingle or problematic for astrometric solutions (L. Lindegren et al. 2018). To identify and remove such UVIT-Gaia sources (see Table 2), first, we gave a constraint on renormalised unit weight error <1.4 (RUWE; L. Lindegren et al. 2018). Then, we followed again all the above two criteria for selecting the most probable SMC stars (see Table 3). In Figure 4(b), we note that the MW stars obtained using only the first criteria (3σ cutoff to the means of Plx: 0.013 mas, $\mu_{\alpha\cos\delta}$: 0.74 mas yr^{-1} and μ_δ: -1.25 mas yr^{-1}) show a spatial distribution like the SMC, even after RUWE constraint. However, the MW stars obtained based on probability and/or G mag cutoff (Ó. Jiménez-Arranz et al. 2023) show more or less uniform distribution, which is the expected spatial distribution of the foreground stars. The numbers of most probable stars obtained after RUWE constraint in NN complete (63,444), optimal NN (62,980), and truncated-optimal NN (62,901) samples are similar. Hereafter, we consider truncated-optimal NN samples (i.e., Gaia cross-matched FUV stars with probability > 31%, $G < 19.5$ mag, and RUWE < 1.4, and listed as probable SMC members (PSMs) in the eighth column of Table 2) for further analysis.
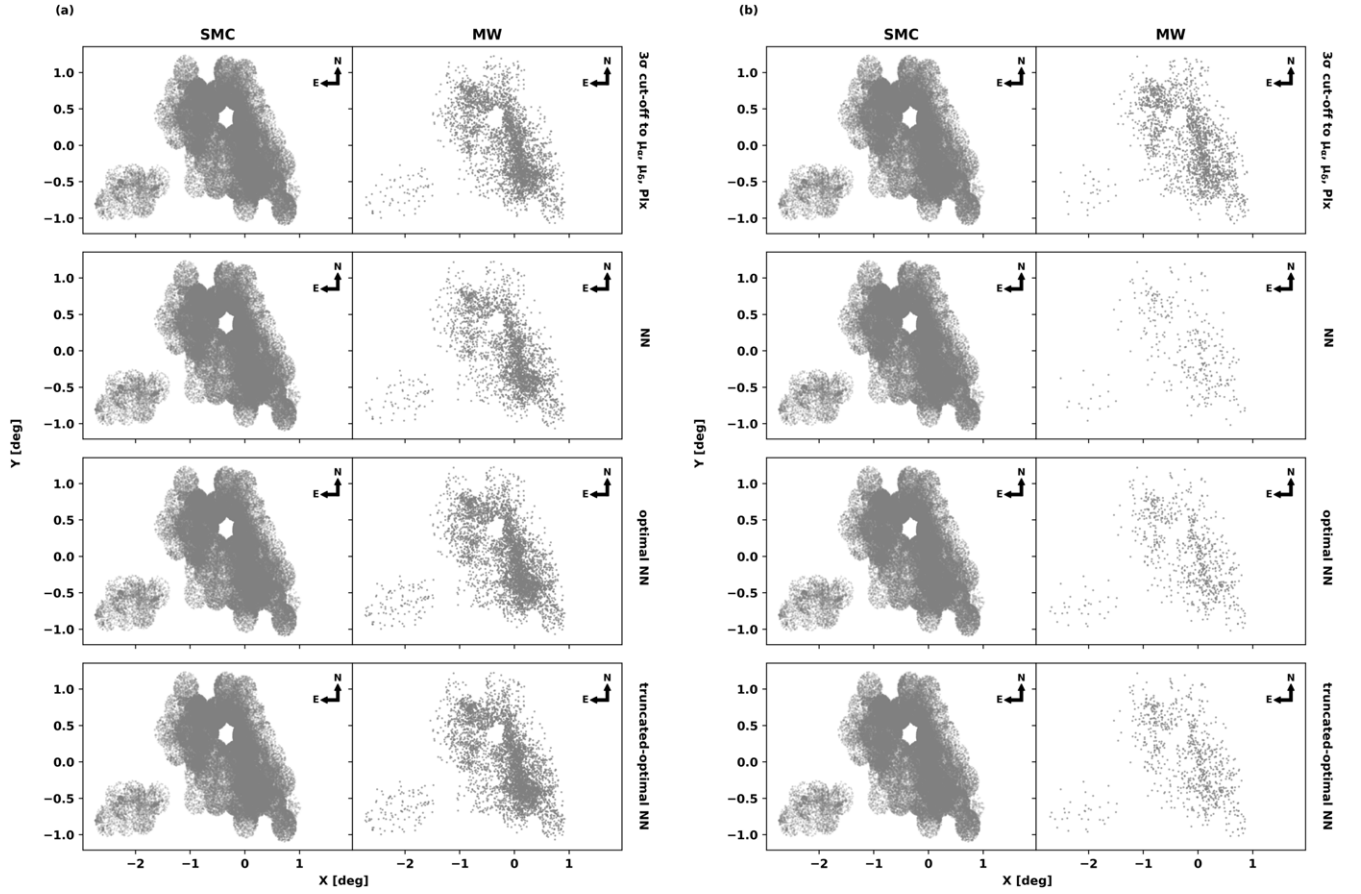
Figure 4. Panels (a) and (b) represent the spatial distribution of probable FUV stars of the SMC and the MW obtained from different methods under two distinct conditions: without RUWE constraints and with a RUWE < 1.4, respectively.

Table 2
FUV Catalog of the Sources Detected in the Direction of the SMC

UVIT_ID	R.A. (deg)	Decl. (deg)	FUV (AB mag)	Error (AB mag)	VMC_PSF_Source_ID	Gaia_DR3_Source_ID	PSM
UVIT00000	10.315324	−73.277606	16.116	0.098	558371534268	4688850813948992896	Y
UVIT00001	09.940444	−73.294990	16.586	0.163	558371499893	4688862942940210304	Y
UVIT00002	10.548706	−73.303662	17.022	0.154	558371482809	4688848855413218688	Y
UVIT00003	10.034966	−73.309045	16.083	0.129	558371472160	4688851054467630464	Y
UVIT00004	10.368390	−73.330106	17.078	0.134	558371430415	4688847446664173568	N

Note. Columns 1–8 of the catalog table present UVIT_ID, spatial coordinates, magnitude in the F172M filter, corresponding fit error in magnitude, VMC_PSF_Source_ID, Gaia_DR3_Source_ID and probable SMC member (PSM), respectively. The complete table is accessible as supplementary online material. Total detected FUV stars: ∼76,800; cross-matched with Gaia: 73,395; cross-matched with VMC: 72,790; cross-matched with both Gaia and VMC: ∼70,900; and not cross-matched with VMC and Gaia: 1456. PSM identified by the truncated-optimal NN with RUWE < 1.4 (62,901 sources) are presented in the last column of the table, where Y and N stand for "Yes" and "No," respectively.

(This table is available in its entirety in machine-readable form in the online article.)

Table 3
Number of Probable FUV Member Sources of the SMC and the MW Obtained Using Different Classification Methods

Methods	SMC	MW	SMC (RUWE <1.4)	MW (RUWE <1.4)
3σ clipping to $\langle\mu_\alpha \cos\delta\rangle$, $\langle\mu_\delta\rangle$, $\langle$Plx$\rangle$	69389	4006	61624	2141
NN complete[a]	70319	3076	63444	321
Optimal NN[a]	68621	4774	62980	785
Truncated-Optimal NN[a]	68540	4855	62901	864

Note.
[a] Ó. Jiménez-Arranz et al. (2023).
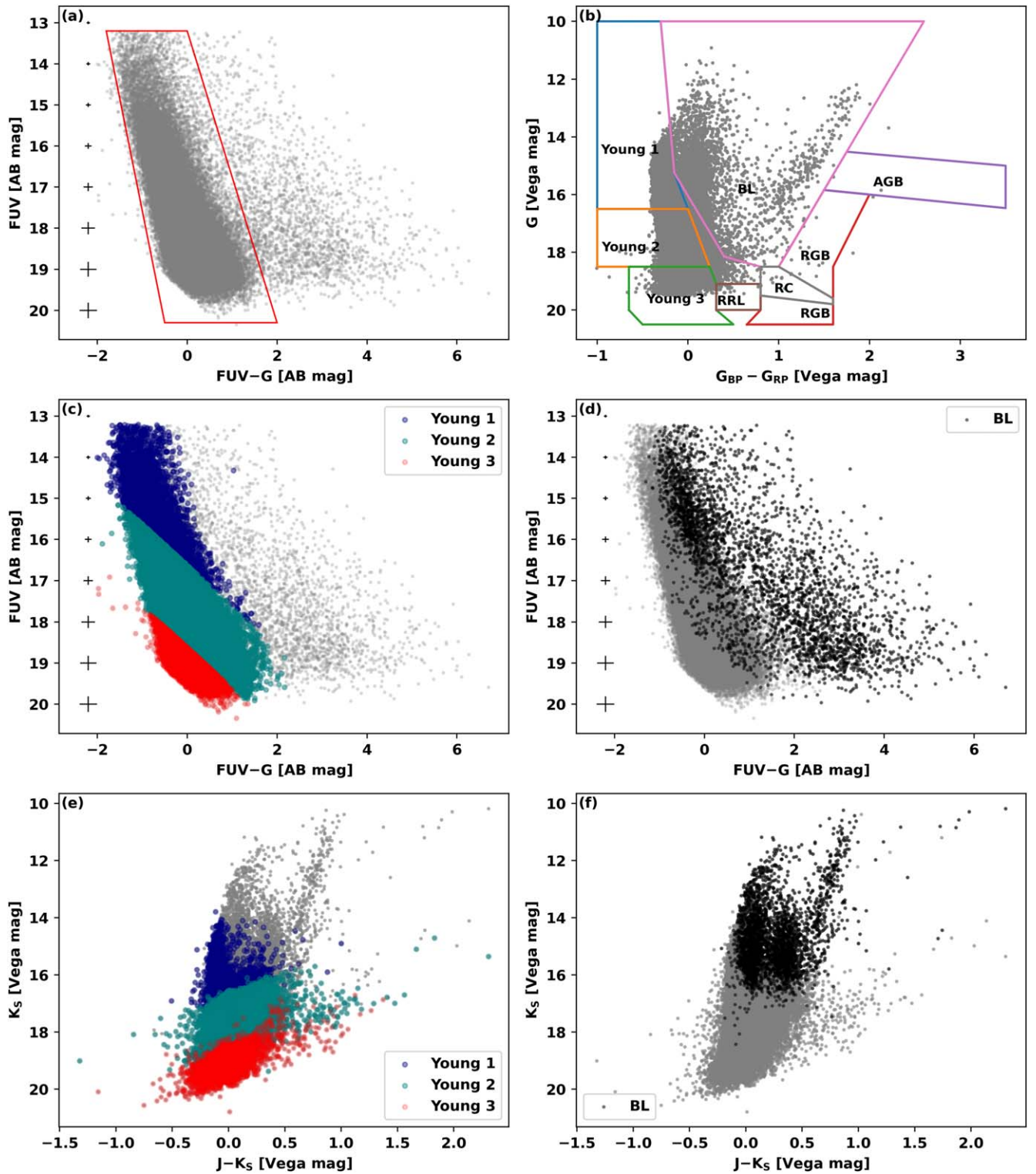
Figure 5. (a) FUV–optical CMD of the SMC sources. The main-sequence branch is shown within a red polygon. (b) Polygons on the optical CMD of the SMC sources representing different populations of the SMC (see right-hand panel of their Figure 2, Gaia Collaboration et al. et al. 2021a). The locations of Young 1, Young 2, Young 3, and BL stars on FUV–optical and IR CMDs are shown in panels (c), (d), (e), and (f), respectively. The error bars (median value) for FUV magnitude and FUV–optical color are shown in black for the FUV–optical CMDs. Gray points are the SMC FUV sources.

3. Color–Magnitude Diagrams

A color–magnitude diagram (CMD) is a useful tool to trace the evolutionary paths of different stellar populations. Our goal is to identify various stellar populations within the SMC based on their location in the FUV–optical CMD. Since the FUV is in AB magnitude, we converted G mag from the Vega magnitude system to the AB magnitude system[7] to create the FUV–optical CMD, as shown in Figure 5(a). To identify various populations, we plotted the Gaia optical CMD (G versus G_{BP}–G_{RP})

---

[7] https://gea.esac.esa.int/archive/documentation/GDR2/Data_processing/chap_cu5pho/sec_cu5pho_calibr/ssec_cu5pho_calibr_extern.html
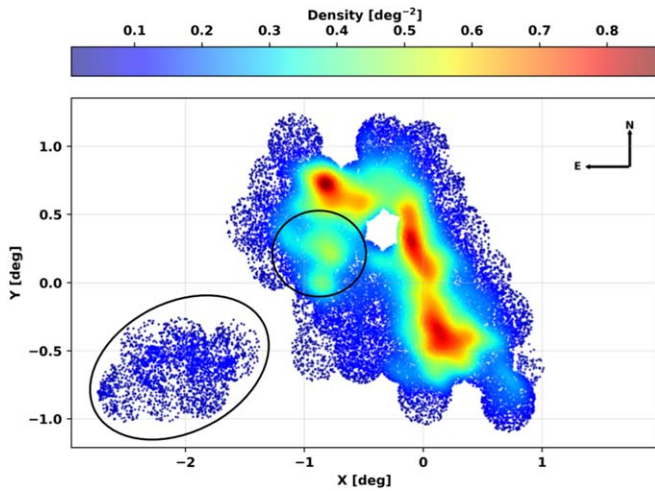
Figure 6. Surface density distribution (KDE; kernel width = 0.1 deg) of the SMC. The color bar represents the density in the unit of deg^{-2}. The black ellipse and circle represent the inner SMC Wing and shell-like structure, respectively.

Table 4
Description and Star Count of Four Young Populations in Our Catalog

Population	Description[a]	N
Young 1	Very young main-sequence (ages < 50 Myr)	4924
Young 2	Young main-sequence (50 < age < 400 Myr)	40,484
Young 3	Intermediate-age main-sequence population (mixed ages reaching up 1–2 Gyr)	11,885
BL	Blue loop (including classical Cepheids)	3584

Note.
[a] The descriptions of the populations are taken from Gaia Collaboration et al. et al. (2021a).

for the 62,901 probable SMC FUV members (see Section 2.5), as shown in Figure 5(b), and identified different populations as described by Gaia Collaboration et al. et al. (2021a). Here, we considered only the young populations (Young 1, Young 2, Young 3, Blue Loop: BL) because they are detected in large numbers (see Figure 5(b)), as listed in Table 4. Since the detected number of red giant branch (RGB), asymptotic giant branch (AGB), red clump (RC), and RR-Lyrae (RRL) are significantly low, we did not consider them for further analysis. Figures 5(c) and (d) show the position of the Young 1, Young 2, Young 3, and BL stars on the FUV–optical CMD of the SMC. We note that Young 1, Young 2, and Young 3 stars have distinct locations on the main-sequence branch with an increasing FUV magnitude (Figure 5(c)), whereas BL stars mostly fall on the redder part of the FUV–optical CMD, with some located on the main-sequence branch (Figure 5(d)).

The young populations defined from Gaia optical CMD (Figure 5(b)) are also plotted in the IR CMD (K_s versus $J–K_s$), as shown in Figures 5(e) and (f), after restricting sources with a maximum photometric error of 0.2 mag in the two IR filters. We compared the positions of the populations in the IR CMD with a similar study by D. El Youssoufi et al. (2019; see Figure 1 in their paper). Our analysis revealed that the BL stars align with the positions of supergiant and giant stars, while the Young 1, Young 2, and Young 3 populations are mainly located on the main-sequence and subgiant branches.

Therefore, we conclude that the detected SMC FUV stars primarily belong to the main-sequence and supergiant/giant stars.

4. Spatial Distribution

The morphological features of the young population in the SMC are examined using the spatial distribution of the FUV stars. It is important to note that the SMC fields exhibit a range of completeness with the FUV magnitude, based on their exposure times and crowding from Figure 3(b). Except two, all fields show their peak FUV magnitude around 19 mag before declining (Figure 3(a)) where completeness is more than ~90%. This suggests that the impact of incompleteness in the morphology based on the FUV stellar density is negligible. The surface stellar density of the SMC is shown in Figure 6, based on a kernel density estimation (KDE) with a kernel width of 0.1 deg, that is sufficient to identify the dense regions. The distribution as seen in Figure 6 is irregular, with an asymmetric young bar and an eastern extension, the inner SMC Wing at $(-2.75 < \Delta\alpha < -1.25, -1 < \Delta\delta < -0.25)$ deg. The young bar has a relatively higher density segregated in three distinct regions in the inner SMC. When there is a continuity between the SW high-density region to the central high-density region, we note a discontinuity in density at $\sim(-0.5, 0.5)$ deg in the NE direction. This stellar density in the young bar is broken (i.e., density is not distributed continuously throughout the SMC bar) and bends toward the east direction. A shell-like structure is detected at $(-0.75, 0.25)$ deg in the east direction toward the SMC Wing.

In order to trace the morphology, the KDE maps of the stellar surface density of Young 1, Young 2, Young 3, and BL stars are shown in Figure 7. These show four distinct dense regions; visually identified and marked as east, NE, center, and SW on the basis of direction, as shown in Figure 7. The relative density in each region varies with population and the Young 2 population is found to closely resemble the overall density map as shown in Figure 6. The maximum range in stellar surface density is seen for the Young 1 population, whereas the other three populations have a reduced but similar range of stellar density values. The densest region of the Young 1 population is in the NE of the bar (Figure 7(a)), whereas the densest BL population is found in the SW (Figure 7(d)) of the bar. The broken bar and the shell-like features are predominantly seen in the Young 2 population. The densest regions of Young 3 are found in the NE as well as at the central part of the bar (see Figure 7(c)).

5. Kinematics

Since the SMC is disturbed due to interactions, the imprint of interactions could be traceable in the motion of the young stars through a kinematic analysis. We performed a 2D kinematic analysis of four populations as well as the five regions using their PM values, and the results are presented here.

The PM distribution of all four populations and the fitted Gaussian curves are shown in Figure 8. The fit parameters, such as the peak and standard deviation values, along with their corresponding errors from the covariance matrix, are listed in Table 5. All the PM distributions had to be fitted with two Gaussian profiles. The Gaussian profiles fitted to Young 1 and BL have slightly differing peaks and widths, whereas those fitted to the Young 2 and 3 populations have significantly
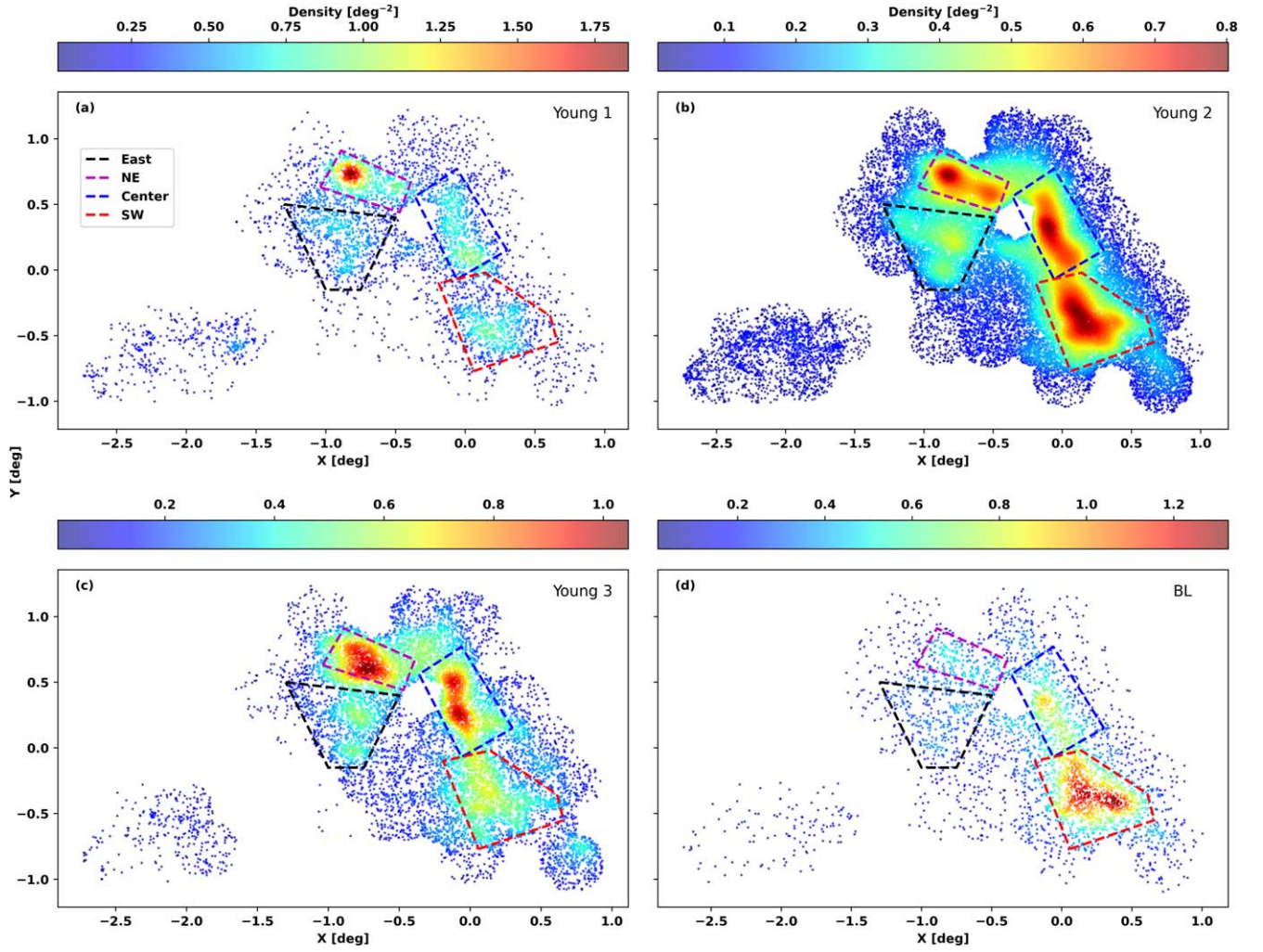
Figure 7. Surface density distribution (KDE; kernel width = 0.1 deg) of Young 1, Young 2, Young 3, and BL populations in (a), (b), (c), and (d), respectively. The color bar represents the density in units of deg^{-2}. Dashed polygons mark four distinct dense regions named east, NE, center, and SW. The labeling in panel (a) is consistent across all panels.

differing widths. The width of the Young 2 and 3 populations suggest that there is a cool component corresponding to a PM distribution with reduced dispersion and a hot component corresponding to a PM distribution with a relatively large dispersion. Interestingly, the two subpopulations of BL and Young 1 exhibit relatively less widths when compared to both the widths of Young 2 and Young 3 profiles. Next, we set out to check if both components of the transverse motion (PM) are contributing to the above-observed differences.

We transformed ($\mu_\alpha \cos\delta$, μ_δ) into the Cartesian plane (μ_x, μ_y) using the conversion equation as defined by Gaia Collaboration et al. (2021a, Equation (2)). After this transformation, we conducted further analysis on the kinematics using the obtained PM values on the X–Y plane, with μ_x and μ_y representing PMRA and PMDec, respectively. Then, we created vector point diagrams (VPDs) for four populations, as shown in Figure 9. VPDs of Young 1 and BL stars (Figure 9) show a spread in PMRA, whereas the PMDec distributions do not. The distributions of Young 2 and Young 3 populations have broad profiles in both PMRA and PMDec distributions. Double Gaussians are well-fitted for the PMRA distributions of Young 1 and BL, while the single Gaussian curves are well-fitted for the rest. The peak and standard deviation values of

these Gaussian fits, along with their corresponding errors obtained from the covariance matrix, are listed in Table 5 (4th to 6th column). The peak PMRA and PMDec values of all the population are similar to each other. The PMRA distribution widths of the Young 1 and BL populations are dissimilar, with the broad distribution showing about thrice the width of the narrow one. We note an increasing width of the PMRA and PMDec distribution from Young 2 to Young 3, which are even larger than the width of the PMRA distribution of Young 1 population and BL stars. We checked the spatial distribution of PMRA for these four populations as shown in Figure 10. We observed a noticeable PMRA gradient, increasing toward the east and NE direction for the Young 1 population in contrast to Young 2 and Young 3. The spatial distribution of PMRA for the BL stars also indicates a similar, though less pronounced, gradient compared to the Young 1 population. We note a distinct pocket of relatively high PMRA in the eastern part of the SMC in the case of the Young 1 population, near the shell-like structure and the inner SMC wing.

We have found two subpopulations in BL and Young 1 based on PMRA distribution (see Figure 9). It is quite interesting to examine whether the subpopulations are located all over the observed SMC or confined to a specific region. To
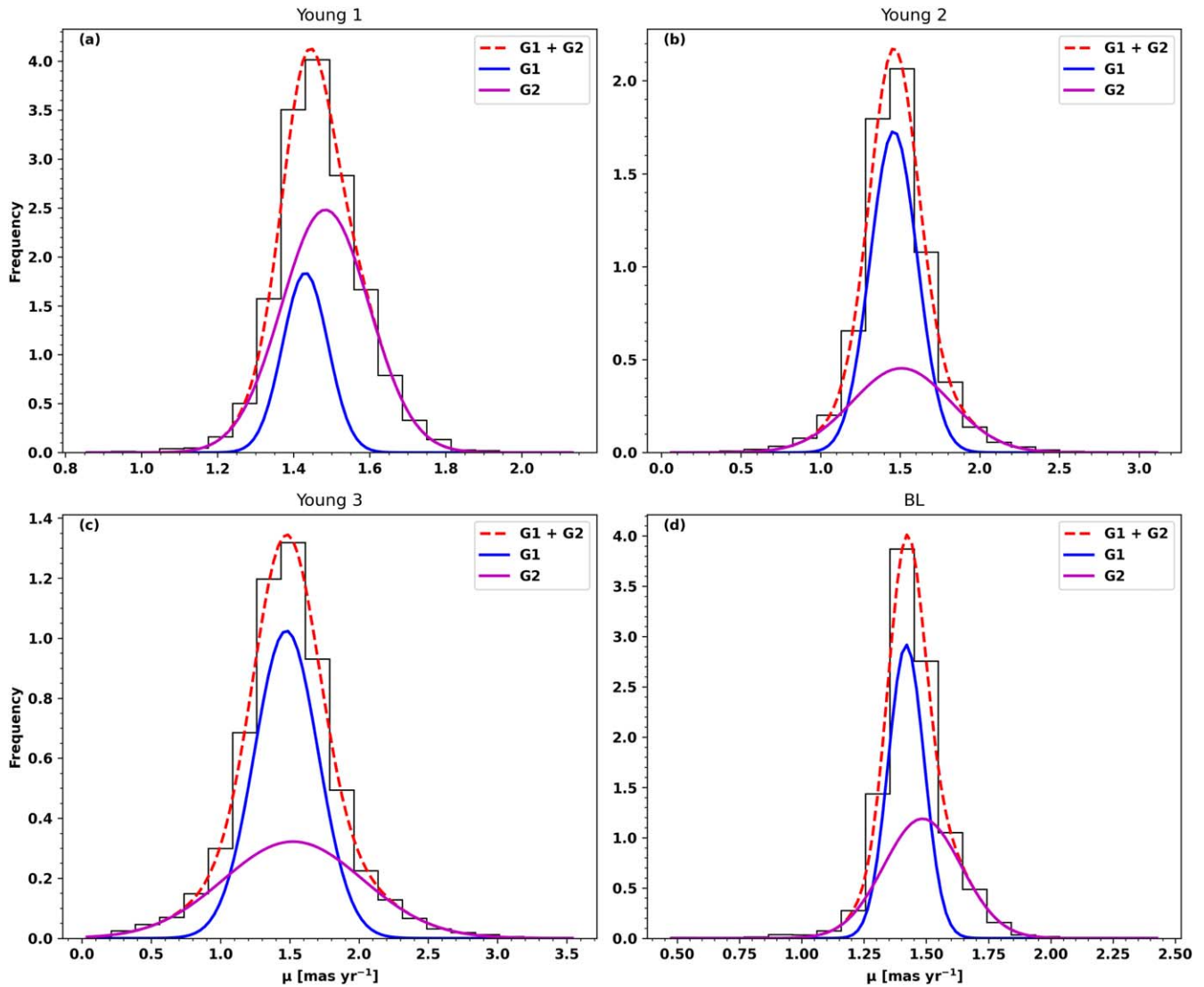
Figure 8. PM distribution of the four young populations. Gaussian 1 (G1), Gaussian 2 (G2), and their sum (G1 + G2) curves are shown in blue, magenta, and red, respectively.

do so, we plotted their VPDs separately for four dense regions and the inner Wing region, as depicted in Figure 11. We clearly see that there are two peaks of PMRA distribution of BL in the east and NE parts of the SMC, although BL stars are more concentrated in the SW part. In the case of the Young 1 population, two possible peaks of PMRA distribution are in the east and NE direction. We note a higher PMRA value in the inner Wing region for both Young 1 and BL populations. We conclude that the two subpopulations with differing PMRA distribution found for Young 1 and BL are mainly located in the east, i.e., the shell-like structure and inner SMC wing. In summary, the analysis points to kinematic differences in PMRA for the young population in east and NE, without any noticeable difference in PMDec.

6. Discussion

The interactions of the SMC with the LMC play a vital role in shaping the morphology of the SMC. In this study, we created an FUV catalog of the SMC obtained from UVIT observations and examined the spatial distribution and kinematics. We found an irregular and clumpy surface density

distribution of the young population of the SMC, which is consistent with the previous studies (e.g., M. R. L. Cioni et al. 2000; D. Zaritsky et al. 2000; D. El Youssoufi et al. 2019).

L. R. Patrick et al. (2022) studied the binary systems that contain red supergiant (RSG) stars of the SMC based on FUV data of 88 RSGs from UVIT. We found a cross-match of 61 FUV sources from our catalog (Table 2) with their RSGs (see their Appendix, Table A2), and the FUV magnitudes of these cross-matched sources are within the error. The RSGs, which are not cross-matched, are either found to be faint or associated with larger errors in FUV magnitude (the cutoff error in FUV magnitude in this study is ≤0.2 mag).

F. Maragoudaki et al. (2001) investigated the spatial distribution of different populations of the SMC. They found that the young population exhibited an asymmetric distribution, unlike the old populations. They attributed this irregularity to the recent interaction between the LMC and the SMC at ∼0.2–0.4 Gyr ago. I. Gonidakis et al. (2009) mapped the spatial distribution of four age groups of the SMC stellar populations and provided the isopleth contour maps using 2MASS data. The spatial distribution of their B and A-type stars are similar

Table 5
Peak and Standard Deviation Values (in the Unit of mas yr^{-1}) of Gaussian Curve Fit on PM, PMRA, and PMDec Distributions, along with Fit Error for Different Young Populations

Populations	Gaussian 1 (PM)		Gaussian 2 (PM)		Gaussian 1 (PMRA)		Gaussian 2 (PMRA)		Gaussian (PMDec)	
	Peak	Std	Peak	Std	Peak	Std	Peak	Std	Peak	Std
Young 1	1.431 ± 0.002	0.060 ± 0.002	1.483 ± 0.003	0.115 ± 0.002	0.662 ± 0.001	0.051 ± 0.002	0.701 ± 0.002	0.142 ± 0.002	-1.288 ± 0.001	0.076 ± 0.001
Young 2	1.460 ± 0.002	0.148 ± 0.004	1.508 ± 0.012	0.308 ± 0.019	0.693 ± 0.004	0.190 ± 0.004	⋯	⋯	-1.281 ± 0.003	0.152 ± 0.003
Young 3	1.475 ± 0.002	0.230 ± 0.005	1.525 ± 0.011	0.504 ± 0.021	0.723 ± 0.006	0.318 ± 0.006	⋯	⋯	-1.266 ± 0.006	0.268 ± 0.006
BL	1.420 ± 0.001	0.072 ± 0.001	1.485 ± 0.003	0.155 ± 0.002	0.670 ± 0.003	0.063 ± 0.006	0.697 ± 0.008	0.166 ± 0.013	-1.261 ± 0.002	0.076 ± 0.002
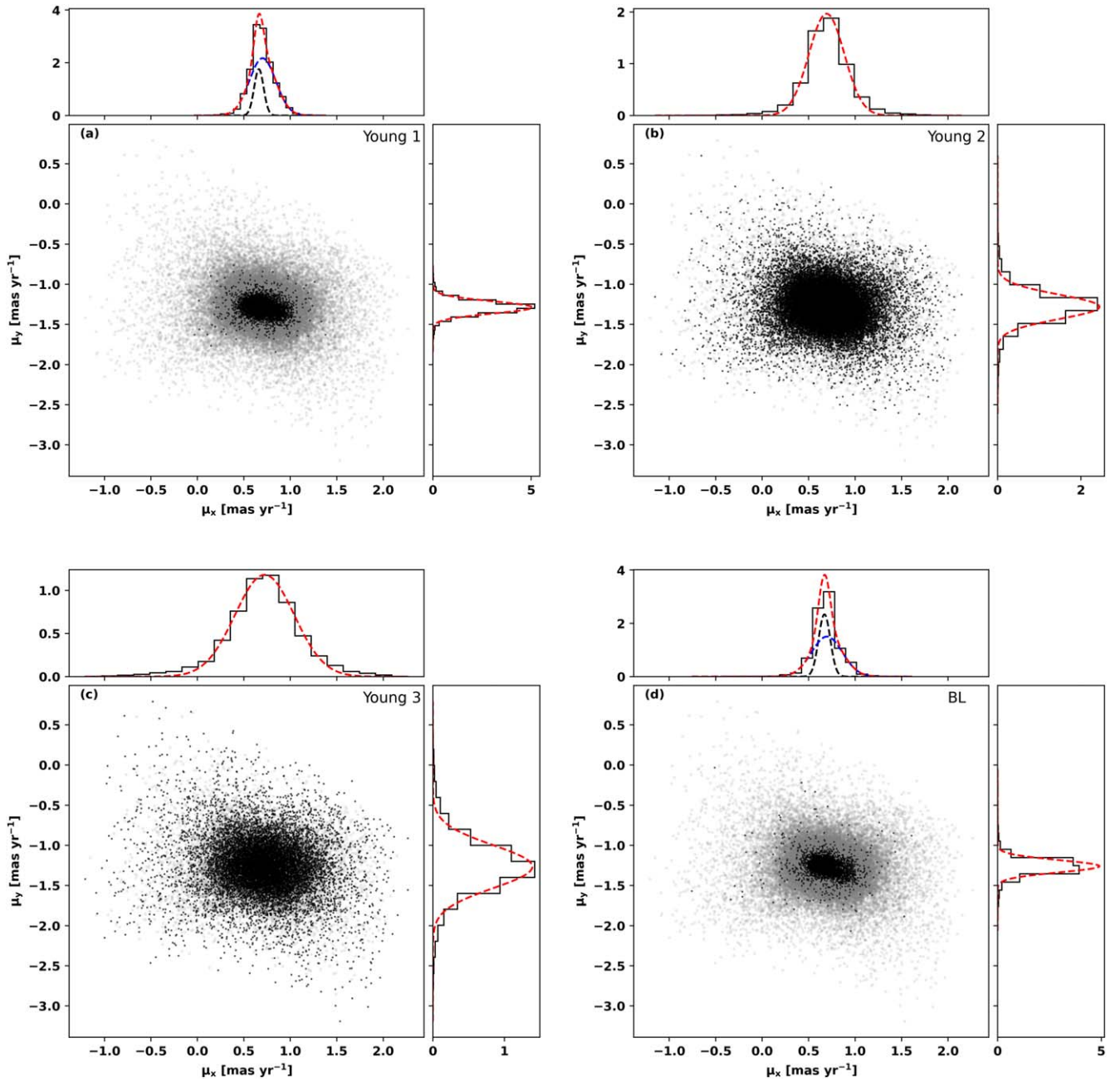
Figure 9. VPDs of four young populations. Distributions of PMRA and PMDec are shown at the top and right-hand side. Gaussian (sum) is shown in red for all panels, while Gaussian 1 and Gaussian 2 are shown in black and blue, respectively, in (a) and (d). Gray points represent the SMC FUV stars.

to the distribution of the Young 2 population. In a study by M. K. Belcheva et al. (2011), iso-density contour maps were used to analyze the morphology of different populations of the Magellanic Clouds. Their spatial distribution for the young stars (see their Figure 4) of the SMC is similar to our result. We also note a shell-like structure at ∼(−0.8, 0.25) deg toward the SMC Wing (Figure 6) that is already mentioned by F. Maragoudaki et al. (2001).

The surface density of the SMC, as well as that of all the four young populations, depict a broken young bar which shows a discontinuity in density at ∼(−0.5, 0.5) deg (see Figures 6 and 7). The presence of the broken bar has previously been reported by D. El Youssoufi et al. (2019; see their Figure 6) and they mention the bending of the bar by about ∼30 deg to the east. In the density distribution of the BL stars, we note a denser region

toward the SW of the bar, which is also found in the density distribution of the supergiant and giant stars by D. El Youssoufi et al. (2019). M. R. L. Cioni et al. (2000) also found an asymmetric distribution of the younger populations (main-sequence and supergiant stars) with protuberance.

In this study, we find that the eastern region and the northeastern regions are mainly populated by Young 1, 2, and 3 stars. The central region predominantly has the Young 2 and 3 populations, whereas the SW has BL stars, and Young 2 and 3 populations. These can be used to trace the recent star formation history of these regions (age < 400 Myr) and study stars of various mass, age, and evolutionary phases.

This catalog has stars up to a mass of ∼30–45 $M_\odot$— photometric mass obtained from a 1 Myr Padova-PARSEC isochrone (A. Bressan et al. 2012) using a distance modulus of
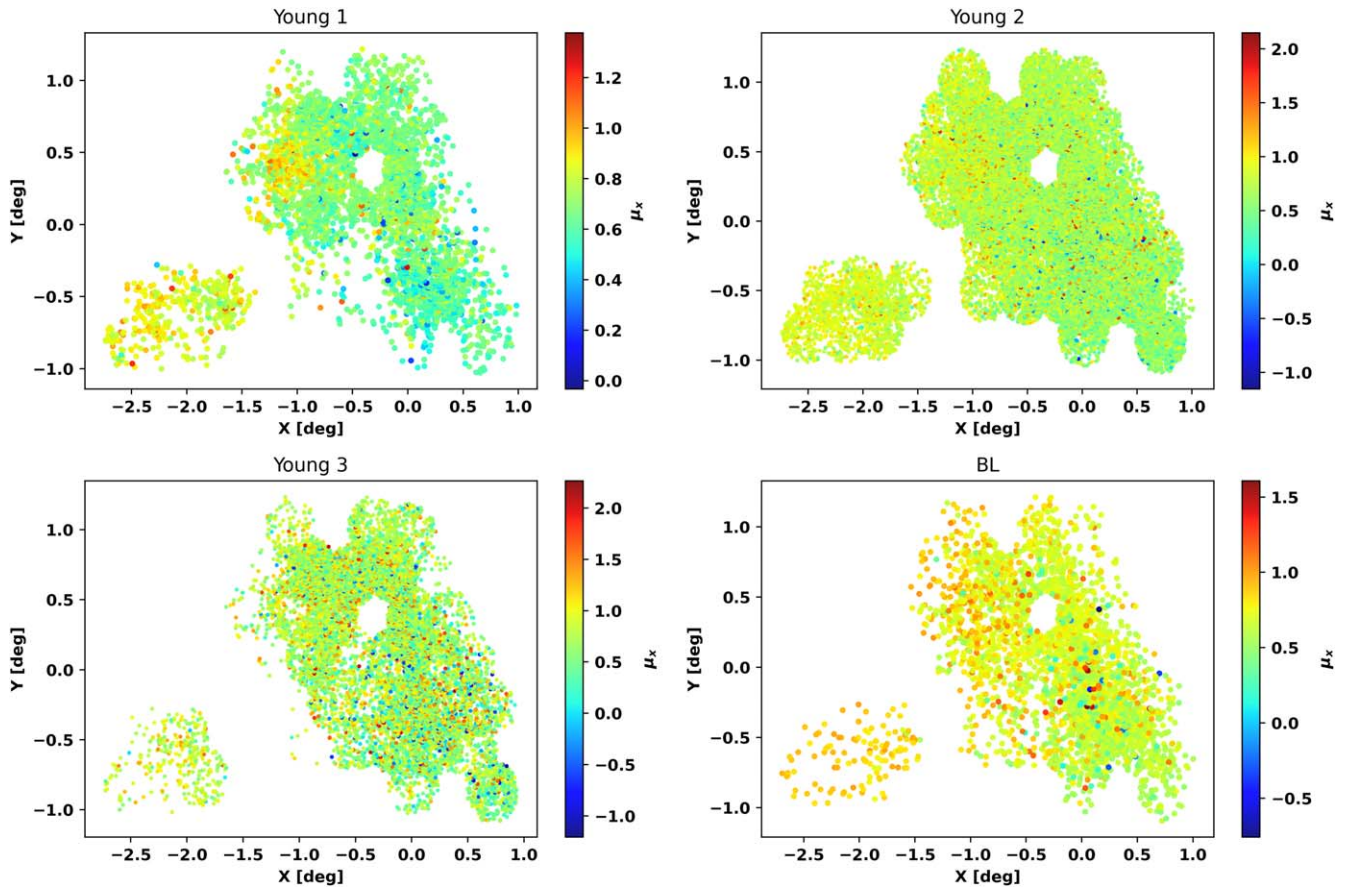
Figure 10. Spatial distribution of PMRA of four young populations.

$m−M = 18.96$ (R. de Grijs & G. Bono 2015) and a metallicity of $Z = 0.002$ dex (S. C. Russell & M. A. Dopita 1992; M. Romaniello et al. 2008; B. Lemasle et al. 2017)—corresponding to an FUV magnitude of ∼13.2. Here, we have used the extinction law from J. A. Cardelli et al. (1989), R_V value of 3.13 (K. D. Gordon et al. 2024), and a range of color excess values; $E(B − V) = 0.05$ mag (mean value; R. Haschke et al. 2011) and 0.1 mag (a higher value around OB stars; K. D. Gordon et al. 2024). Since massive stars ($M > 8 M_⊙$) are likely progenitors of supernovae, we show the spatial distribution of stars brighter than 15 mag in FUV corresponding to a mass of ∼8 $M_⊙$, as shown in Figure 12. The spatial distribution of these massive stars (∼2200) is similar to the distribution of Hα of the SMC (J. E. Gaustad et al. 2001; N. M. McClure-Griffiths et al. 2018). These are the sites of high-mass star formation in the inner SMC. These FUV bright stars, as well as their location, will be of interest to various ongoing studies, such as binary at low metallicity by T. Shenar et al. (2024), B-type supergiants by T. N. Parsons et al. (2024), and many other studies of massive stars.

The PMRA and PMDec values estimated for the young populations are well matched with the previous studies (E. Costa et al. 2009; R. P. van der Marel & J. Sahlmann 2016; P. Zivick et al. 2018; F. Niederhofer et al. 2021). From the PMRA distribution, we found that Young 1 and BL stars have two types of subpopulations, which are mainly located in the east and NE direction of the SMC (see Figures 9, 11). However, the widths of the PM distribution of both of the populations are relatively low, indicating that these subpopulations are relatively undisturbed (as seen in Figure 8 and Table 5). We also note an increase in PMRA (not found in
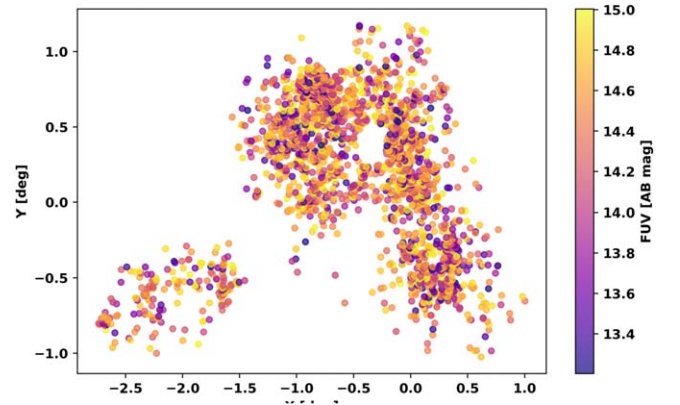
PMDec) for BL and Young 1 populations in the eastern SMC. A similar pattern in the PM of young stars in the SMC was reported by F. Niederhofer et al. (2021). However, our findings confirm that this stretching in PM is predominantly due to the motion of young stars in the R.A. direction. Additionally, M. De Leo et al. (2020), in their analysis (see Figure 10), also observed increased PMRA values for RGB stars in the eastern region of the SMC. C. E. Murray et al. (2019) identified a similar gradient in the residual PM of 143 massive stars, whose radial velocities are aligned with H I gas peaks. A recent study by A. Almeida et al. (2024) found a similar pattern in the radial velocity and proper motion of RGB stars. This study suggests that stars located on the eastern side of the SMC are part of material pulled out from the central SMC due to its tidal interaction with the LMC. However, these higher PMRA values are found within the 2 deg of the SMC, and are hence unlikely to be connected to the foreground population found by A. O. Omkumar et al. (2021) and D. James et al. (2021; using RC and RGB tracers, respectively) in the east of the SMC beyond 2 deg from the SMC center. Overall, our result of the PMRA gradient observed in the Young 1 and BL populations indicates that stars younger than 250 Myr are being stretched toward the LMC, likely as a consequence of the recent LMC-SMC interaction.

In order to check whether we can trace the impact of the recent LMC-SMC interaction at 150–300 Myr ago (M. J. Irwin et al. 1985; G. Besla et al. 2012; Y. Choi et al. 2022) in the motion of the young population, we overlaid a 150 Myr Padova-PARSEC isochrone (A. Bressan et al. 2012) considering a distance modulus of $m−M = 18.96$ (R. de Grijs &
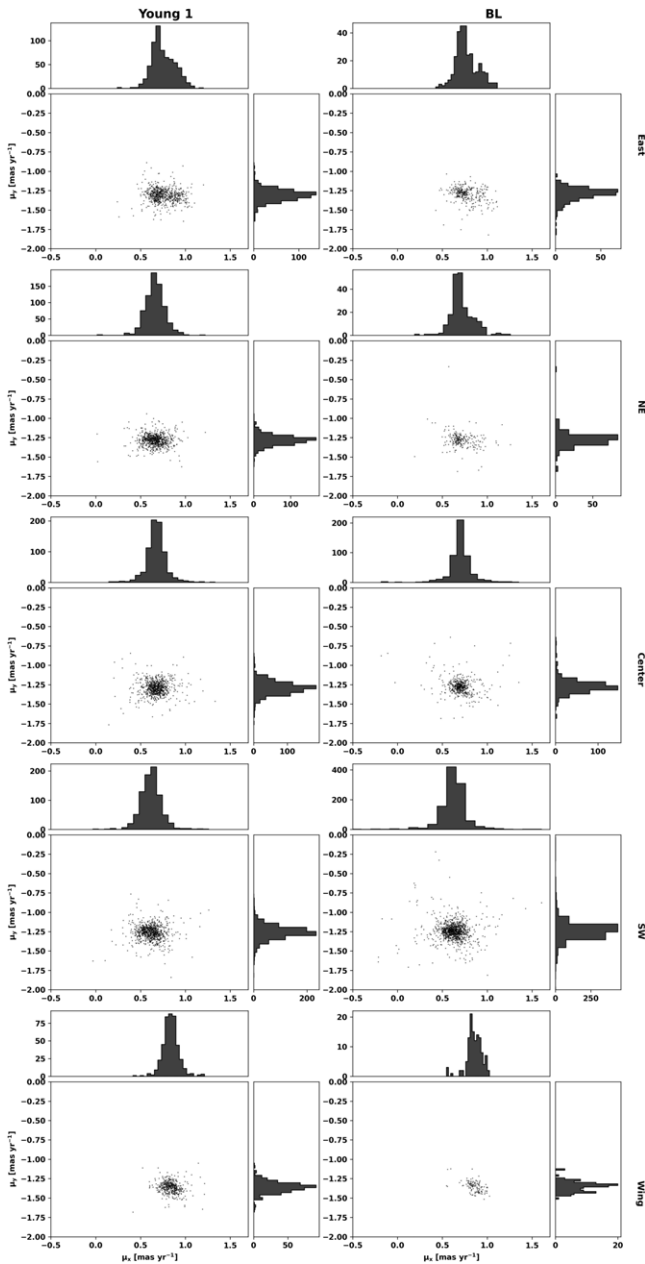
Figure 11. VPDs of four dense and inner Wing regions of Young 1 and BL stars. Distributions of PMRA and PMDec are shown at the top and right-hand side, respectively.

Figure 12. Spatial distribution of the SMC FUV stars brighter than 15 mag corresponding to a photometric mass $>8 M_\odot$.

G. Bono 2015) on the Gaia optical CMD, as shown in Figure 13(a), to separate populations born before and after the interaction. We can see that BL stars have both types of populations: (1) before interaction (age $\leqslant 150$ Myr) and (2) during/after the interaction (age > 150 Myr). From the Gaussian curve fit to the PM distribution of these two populations of BL stars as shown in Figure 13(b), we determined the peak and sigma values as follows: for the BL population with age $\leqslant 150$ Myr, $(\mu_1, \sigma_1) = (1.420 \pm 0.002, 0.070 \pm 0.003)$ and $(\mu_2, \sigma_2) = (1.504 \pm 0.024, 0.142 \pm 0.011)$, and for the BL population with age > 150 Myr, $(\mu, \sigma) = (1.436 \pm 0.010, 0.189 \pm 0.010)$. BL stars with age $\leqslant 150$ Myr show a peaked narrow distribution that has contributions from two populations with different transverse motions. The broader distribution of the above two appears to be similar to that of BL population with

age > 150 Myr. Since the number of stars of the older BL population is not statistically significant, we will not discuss this population further but provide its VPD, as shown in Figure 13(d). The peak and standard deviation of PMDec distribution for the two BL populations with age $\leqslant 150$ Myr and > 150 Myr are $(-1.260 \pm 0.002, 0.067 \pm 0.002)$ and $(-1.252 \pm 0.006, 0.157 \pm 0.006)$, respectively. The Gaussian curve fits for PMRA distribution to these are listed in Table 6. We note from PMRA distribution, as shown in Figure 13(c), that BL stars younger than 150 Myr have three subpopulations with slightly different peaks and widths in PMRA (Table 6). We checked the spatial distribution of PMRA of the BL stars (age $\leqslant 150$ Myr and > 150 Myr) as shown in Figures 13(e) and (f). We found that there is a gradient in PMRA for the BL stars with age $\leqslant 150$ Myr, unlike the older BL stars. The gradient in PMRA is in the direction from SW to NE and east. We have already found that the Young 1 population that is also formed after the recent interaction shows a very similar kinematic signature. We conclude that the younger subpopulation of BL stars and the Young 1 population bear the kinematic signature of the recent LMC-SMC interaction. This signature is in the PMRA distribution and we do not detect any perturbation in the PMDec distribution. This is an important pointer that can constrain the models of the LMC-SMC interaction.

Four regions of the SMC (bar) were observed by the UIT[8] (R. H. Cornett et al. 1997). We have cross-matched the UVIT catalog with the UIT catalog (FUV: 1620 Å) of the SMC with search radii of $2''$ and $1''$ (spatial resolution of UIT is $3''$) and found ~ 1700 and ~ 550 common sources, respectively. Figure 14 shows the relation between the UVIT and UIT magnitudes, and their fluxes are found to be well matched in a study by A. Subramaniam et al. (2016b). Cross-matching the common sources with the SIMBAD database revealed that many of these sources are eclipsing binaries, emission-line stars, etc., and are marked in the figure. Differences in the magnitudes between the two catalogs arise from variations in filter wavelengths and widths, magnitude system, and the spatial resolution of UVIT and UIT and variable nature of some sources.

The SMC FUV sources are younger than 400 Myr (S. Hota et al. 2024). Various studies have indicated that massive stars are often found in binary or higher multiple systems (B. D. Mason et al. 1998; B. García & J. C. Mermilliod 2001; H. Sana et al. 2014; M. Moe & R. Di Stefano 2017). It is estimated that

---

[8] Of the four UIT fields, three overlap with UVIT fields, while one lies in a gap within the UVIT observed area.
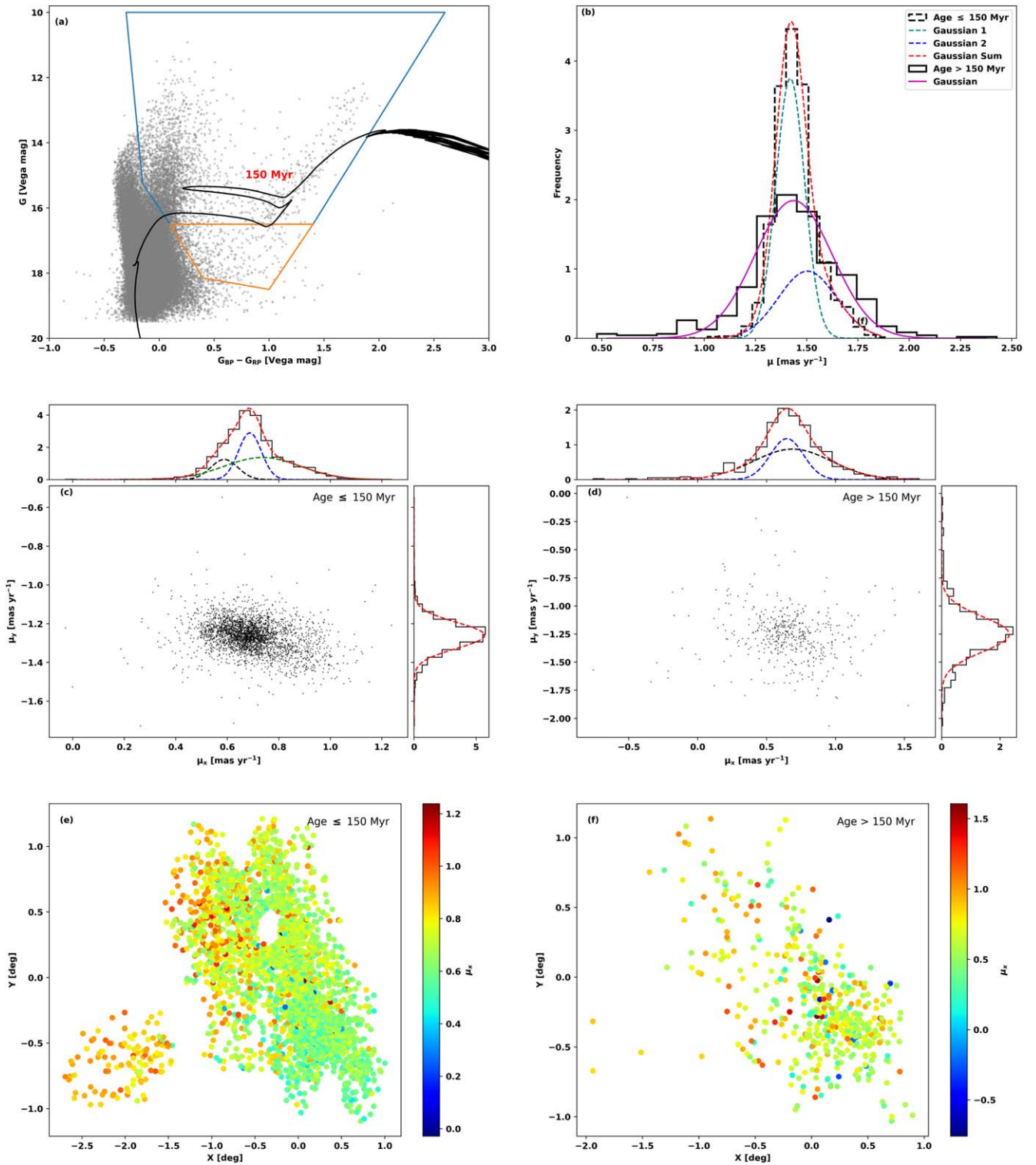
Figure 13. (a) BL stars on the optical CMD. Blue and orange polygons denote the BL stars with age ⩽150 Myr and >150 Myr, respectively. (b) Gaussian curve fits the PM distribution. (c) and (d) VPDs with PMRA and PMDec distribution at the top and right, respectively. (e) and (f) present the spatial distribution of PMRA of two BL subpopulations (age ⩽150 Myr and >150 Myr).

approximately 70% of close binary systems (H. Sana et al. 2012; H. A. Kobulnicky et al. 2014) are likely to interact, impacting stellar evolution, apart from leading to the end stages of a massive star, such as a supernova explosion (P. Podsiadlowski et al. 1992; S. E. de Mink et al. 2013; O. De Marco & R. G. Izzard 2017). They also have the potential to form double compact object binaries (P. Marchant et al. 2017). In our future

work, we plan to identify binaries through multiband photometry and characterize them, apart from estimating the properties of single stars. The catalog presented in this work will be a very useful resource to study the FUV properties of various exotic populations such as the high-mass X-ray binaries, Wolf-Rayet stars, O/B emission-line stars, Be-X-ray binaries, etc. This photometric catalog will also be quite a useful resource to plan

BL Population	Gaussian 1		Gaussian 2		Gaussian 3	
	Peak (mas yr^{-1})	Std (mas yr^{-1})	Peak (mas yr^{-1})	Std (mas yr^{-1})	Peak (mas yr^{-1})	Std (mas yr^{-1})
age $\leqslant$ 150 Myr	0.588 ± 0.013	0.053 ± 0.008	0.688 ± 0.004	0.045 ± 0.002	0.736 ± 0.008	0.148 ± 0.004
age > 150 Myr	0.688 ± 0.023	0.283 ± 0.036	0.647 ± 0.010	0.120 ± 0.018	⋯	⋯
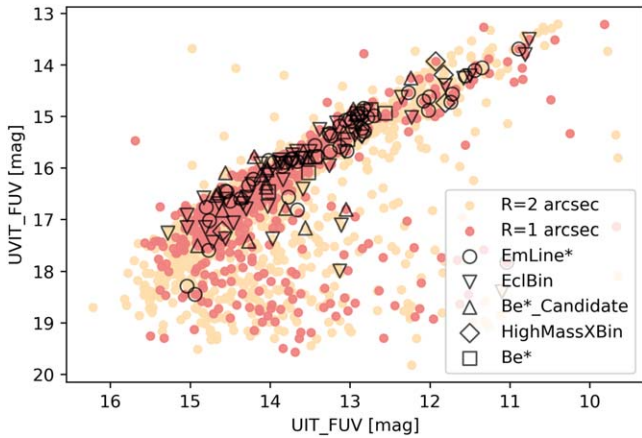
Figure 14. UVIT and UIT FUV magnitudes of common sources (for search radii of 2″ and 1″). Different markers represent UVIT-UIT-SIMBAD stars classified as emission-line stars, eclipsing binaries, Be star candidates, high-mass X-ray binaries, and Be stars.

photometric/spectroscopic observations of future space-based observatories, such as the Ultraviolet Explorer (UVEX; S. R. Kulkarni et al. 2021) and the Indian Spectroscopic and Imaging Space Telescope (INSIST; A. Subramaniam 2022; S. Sriram et al. 2023).

7. Summary and Conclusions

In this study, we present a FUV catalog of the SMC obtained using the UVIT/AstroSat, based on observations of 39 pointings of UVIT in the filter F172M. The catalog contains ∼76,800 sources along with their IDs in Gaia and VMC. This catalog will be an excellent resource for various studies of young and massive stellar populations in the SMC. We also provide the data completeness as a function of magnitude for the observed regions.

Applying different classification methods to get the most probable SMC stars, we found that RUWE constraint is required for better MW decontamination. We adopt the Truncated-Optimal NN of Ó. Jiménez-Arranz et al. (2023) and RUWE < 1.4 cutoff to identify the probable SMC population consisting of 62,901 stars. The spatial as well as kinematical properties of this population as found in this study are summarized below:

1. FUV stars in the catalog are mainly main-sequence, giant, and subgiant stars, as found from the CMDs (Gaia optical, FUV–optical, and VMC IR CMDs).
2. There are about ∼2200 stars that are brighter than 15 mag in FUV, corresponding to a photometric mass of $M > 8M_\odot$. This catalog is therefore an important resource to study massive stars in a low metallicity environment.
3. Stellar surface density distribution is found to be clumpy. The distribution traces three morphological features, such

as the inner SMC Wing, a broken bar, and a shell-like structure. We also find a high concentration of FUV stars in the SW of the bar.
4. The morphology as a function of stellar population is studied through KDE plots. From the KDE plots of Young 1, Young 2, Young 3, and BL stars, we find that the morphology varies with population. The density distribution of Young 2 stars has a close resemblance to the overall density while Young 1 and BL stars are concentrated at the NE and SW of the bar, respectively. The densest regions of Young 3 stars are located in the northeast and at the central part of the bar.
5. The kinematic properties of the above population suggest that all populations show two kinematically distinct subpopulations. The Young 2 and 3 stars show kinematically cool, less dispersed (with a narrower width in the PM distribution) and hot, highly dispersed (with a broad PM distribution) subpopulations, whereas the Young 1 and BL stars show two kinematically distinct cool populations.
6. The VPDs suggest that the kinematically distinct subpopulations of Young 1 and BL stars differ in PMRA, but have similar PMDec distribution. The spatial distribution of PMRA of Young 1 and BL stars shows a gradient that increases toward the eastern SMC, mainly located in the shell-like structure (east) and NE part of the bar.
7. The kinematic analysis of this study points to a specific disturbance for stars younger than ∼150 Myr in the PMRA, with no significant disturbance in the PMDec. This can place strong constraints on the details of the recent LMC-SMC interaction.
8. The probable SMC members (∼62,900) with FUV magnitudes will be very useful to the study of massive young stars in the low metallicity and kinematically perturbed environment of the SMC.

ORCID iDs

Sipra Hota ● https://orcid.org/0009-0000-3938-162X
Annapurni Subramaniam ● https://orcid.org/0000-0003-4612-620X
Prasanta K. Nayak ● https://orcid.org/0000-0002-4638-1035
Smitha Subramanian ● https://orcid.org/0000-0002-5331-6098

References

Almeida, A., Majewski, S. R., Nidever, D. L., et al. 2024, MNRAS, 529, 3858
Astropy Collaboration, Robitaille, T. P., Tollerud, E. J., et al. 2013, A&A, 558, A33
Belcheva, M. K., Livanou, E., Kontizas, M., Nikolov, G. B., & Kontizas, E. 2011, A&A, 527, A31
Belokurov, V., Erkal, D., Deason, A. J., et al. 2017, MNRAS, 466, 4711
Belokurov, V. A., & Erkal, D. 2019, MNRAS, 482, L9
Besla, G., Kallivayalil, N., Hernquist, L., et al. 2007, ApJ, 668, 949
Besla, G., Kallivayalil, N., Hernquist, L., et al. 2012, MNRAS, 421, 2109
Bonanos, A. Z., Lennon, D. J., Köhlinger, F., et al. 2010, AJ, 140, 416
Bot, C., Boulanger, F., Lagache, G., Cambrésy, L., & Egret, D. 2004, A&A, 423, 567
Bressan, A., Marigo, P., Girardi, L., et al. 2012, MNRAS, 427, 127
Cardelli, J. A., Clayton, G. C., & Mathis, J. S. 1989, ApJ, 345, 245
Chandra, V., Naidu, R. P., Conroy, C., et al. 2023, ApJ, 956, 110
Choi, Y., Olsen, K. A. G., Besla, G., et al. 2022, ApJ, 927, 153
Cioni, M. R. L., Clementini, G., Girardi, L., et al. 2011, A&A, 527, A116
Cioni, M. R. L., Habing, H. J., & Israel, F. P. 2000, A&A, 358, L9
Cohen, M., Wheaton, W. A., & Megeath, S. T. 2003, AJ, 126, 1090
Cornett, R. H., Greason, M. R., Hill, J. K., et al. 1997, AJ, 113, 1011
Cornett, R. H., Hill, J. K., Bohlin, R. C., et al. 1994, ApJL, 430, L117
Costa, E., Méndez, R. A., Pedreros, M. H., et al. 2009, AJ, 137, 4339
Cullinane, L. R., Mackey, A. D., DaCosta, G. S., Koposov, S. E., & Erkal, D. 2023, MNRAS, 518, L25
de Grijs, R., & Bono, G. 2015, AJ, 149, 179
de Grijs, R., Wicker, J. E., & Bono, G. 2014, AJ, 147, 122
De Leo, M., Carrera, R., Noël, N. E. D., et al. 2020, MNRAS, 495, 98
De Marco, O., & Izzard, R. G. 2017, PASA, 34, e001
de Mink, S. E., Langer, N., Izzard, R. G., Sana, H., & de Koter, A. 2013, ApJ, 764, 166
de Vaucouleurs, G., & Freeman, K. C. 1972, VA, 14, 163
Devaraj, A., Joseph, P., Stalin, C. S., Tandon, S. N., & Ghosh, S. K. 2023, ApJ, 946, 65
Dias, B., Angelo, M. S., Oliveira, R. A. P., et al. 2021, A&A, 647, L9
Dias, B., Kerber, L., Barbuy, B., Bica, E., & Ortolani, S. 2016, A&A, 591, A11
Dias, B., Parisi, M. C., Angelo, M., et al. 2022, MNRAS, 512, 4334
D'Onghia, E., & Fox, A. J. 2016, ARA&A, 54, 363
El Youssoufi, D., Cioni, a.-L., Bell, C. P. M., et al. 2019, MNRAS, 490, 1076
Gaia Collaboration, Brown, A. G. A., Vallenari, A., et al. 2021b, A&A, 649, A1
Gaia Collaboration, Luri, X., Chemin, L., et al. 2021a, A&A, 649, A7
Gaia Collaboration, Prusti, T., de Bruijne, J. H. J., et al. 2016, A&A, 595, A1
Gaia Collaboration, Vallenari, A., & Brown, A. G. A. 2023, A&A, 674, A1
García, B., & Mermilliod, J. C. 2001, A&A, 368, 122
Gardiner, L. T., & Hatzidimitriou, D. 1992, MNRAS, 257, 195
Gardiner, L. T., Sawa, T., & Fujimoto, M. 1994, MNRAS, 266, 567

Gaustad, J. E., McCullough, P. R., Rosing, W., & Van Buren, D. 2001, PASP, 113, 1326
Gehrels, N., Chincarini, G., Giommi, P., et al. 2004, ApJ, 611, 1005
Glatt, K., Grebel, E. K., & Koch, A. 2010, A&A, 517, A50
Gonidakis, I., Livanou, E., Kontizas, E., et al. 2009, A&A, 496, 375
Gordon, K. D., Fitzpatrick, E. L., Massa, D., et al. 2024, ApJ, 970, 51
Gordon, K. D., Meixner, M., Meade, M. R., et al. 2011, AJ, 142, 102
Graczyk, D., Pietrzyński, G., Thompson, I. B., et al. 2020, ApJ, 904, 13
Harris, C. R., Millman, K. J., van der Walt, S. J., et al. 2020, Natur, 585, 357
Harris, J., & Zaritsky, D. 2004, AJ, 127, 1531
Haschke, R., Grebel, E. K., & Duffau, S. 2011, AJ, 141, 158
Haschke, R., Grebel, E. K., & Duffau, S. 2012, AJ, 144, 106
Hindman, J. V., Kerr, F. J., & McGee, R. X. 1963, AuJPh, 16, 570
Hota, S., Subramaniam, A., Dhanush, S. R., Cioni, M. R. L., & Subramanian, S. 2024, MNRAS, 532, 322
Hu, Y., Deng, L., de Grijs, R., & Liu, Q. 2011, PASP, 123, 107
Hunter, J. D. 2007, CSE, 9, 90
Indu, G., & Subramaniam, A. 2011, A&A, 535, A115
Irwin, M. J., Kunkel, W. E., & Demers, S. 1985, Natur, 318, 160
James, D., Subramanian, S., Omkumar, A. O., et al. 2021, MNRAS, 508, 5854
Jiménez-Arranz, Ó., Romero-Gómez, M., Luri, X., & Masana, E. 2023, A&A, 672, A65
Joshi, Y. C., & Panchal, A. 2019, A&A, 628, A51
Kallivayalil, N., van der Marel, R. P., & Alcock, C. 2006, ApJ, 652, 1213
Kobulnicky, H. A., Kiminki, D. C., Lundquist, M. J., et al. 2014, ApJS, 213, 34
Kulkarni, S. R., Harrison, F. A., Grefenstette, B. W., et al. 2021, arXiv:2111.15608
Kumar, A., Ghosh, S. K., Hutchings, J., et al. 2012, Proc. SPIE, 84431N, 1375
Leahy, D. A., Postma, J., Chen, Y., & Buick, M. 2020, ApJS, 247, 47
Lemasle, B., Groenewegen, M. A. T., Grebel, E. K., et al. 2017, A&A, 608, A85
Lindegren, L., Hernández, J., Bombrun, A., et al. 2018, A&A, 616, A2
Liu, Y.-Z. 1992, A&A, 257, 505
Lucchini, S., D'Onghia, E., Fox, A. J., et al. 2020, Natur, 585, 203
Mackey, D., Koposov, S., Da Costa, G., et al. 2018, ApJL, 858, L21
Maragoudaki, F., Kontizas, M., Morgan, D. H., et al. 2001, A&A, 379, 864
Marchant, P., Langer, N., Podsiadlowski, P., et al. 2017, A&A, 604, A55
Martínez-Delgado, D., Vivas, A. K., Grebel, E. K., et al. 2019, A&A, 631, A98
Mason, B. D., Gies, D. R., Hartkopf, W. I., et al. 1998, AJ, 115, 821
Massana, P., Noël, N. E. D., Nidever, D. L., et al. 2020, MNRAS, 498, 1034
McClure-Griffiths, N. M., Dénes, H., Dickey, J. M., et al. 2018, NatAs, 2, 901
Moe, M., & Di Stefano, R. 2017, ApJS, 230, 15
Muller, E., & Bekki, K. 2007, MNRAS, 381, L11
Murray, C. E., Hasselquist, S., Peek, J. E. G., et al. 2024, ApJ, 962, 120
Murray, C. E., Peek, J. E. G., Di Teodoro, E. M., et al. 2019, ApJ, 887, 267
Nayak, P. K., Subramaniam, A., Choudhury, S., & Sagar, R. 2018, A&A, 616, A187
Nidever, D. L., Majewski, S. R., & Burton, W. B. 2008, ApJ, 679, 432
Nidever, D. L., Majewski, S. R., Burton, W. B., & Nigra, L. 2010, ApJ, 723, 1618
Nidever, D. L., Olsen, K., Choi, Y., et al. 2021, AJ, 161, 74
Nidever, D. L., Olsen, K., Walker, A. R., et al. 2017, AJ, 154, 199
Niederhofer, F., Cioni, a.-L., Rubele, S., et al. 2021, MNRAS, 502, 2859
Niederhofer, F., Cioni, M. R. L., Rubele, S., et al. 2018, A&A, 613, L8
Omkumar, A. O., Subramanian, S., Niederhofer, F., et al. 2021, MNRAS, 500, 2757
Parsons, T. N., Prinja, R. K., Bernini-Peron, M., et al. 2024, MNRAS, 527, 11422
Patrick, L. R., Thilker, D., Lennon, D. J., et al. 2022, MNRAS, 513, 5847
Pieres, A., Santiago, B. X., Drlica-Wagner, A., et al. 2017, MNRAS, 468, 1349
Pietrzyński, G., Graczyk, D., Gallenne, A., et al. 2019, Natur, 567, 200
Podsiadlowski, P., Joss, P. C., & Hsu, J. J. L. 1992, ApJ, 391, 246
Postma, J., Hutchings, J. B., & Leahy, D. 2011, PASP, 123, 833
Postma, J. E., & Leahy, D. 2017, PASP, 129, 115002
Postma, J. E., & Leahy, D. 2021, JApA, 42, 30
Putman, M. E., Gibson, B. K., Staveley-Smith, L., et al. 1998, Natur, 394, 752
Ripepi, V., Cioni, a. L., Moretti, M. I., et al. 2017, MNRAS, 472, 808
Romaniello, M., Primas, F., Mottini, M., et al. 2008, A&A, 488, 731
Rubele, S., Girardi, L., Kerber, L., et al. 2015, MNRAS, 449, 639
Rubele, S., Pastorelli, G., Girardi, L., et al. 2018, MNRAS, 478, 5017
Russell, S. C., & Dopita, M. A. 1992, ApJ, 384, 508
Sagar, R., & Richtler, T. 1991, A&A, 250, 324
Sahu, S., Subramaniam, A., Singh, G., et al. 2022, MNRAS, 514, 1122
Sakowska, J. D., Noël, N. E. D., Ruiz-Lara, T., et al. 2024, MNRAS, 532, 4272
Sana, H., de Mink, S. E., de Koter, A., et al. 2012, Sci, 337, 444

Sana, H., Le Bouquin, J. B., Lacour, S., et al. 2014, ApJS, 215, 15
Scowcroft, V., Freedman, W. L., Madore, B. F., et al. 2016, ApJ, 816, 49
Shenar, T., Bodensteiner, J., Sana, H., et al. 2024, A&A, 690, A289
Simons, R., Thilker, D., Bianchi, L., & Wyder, T. 2014, AdSpR, 53, 939
Sriram, S., Valsan, V., Subramaniam, A., et al. 2023, JApA, 44, 55
Stanimirović, S., Staveley-Smith, L., & Jones, P. A. 2004, ApJ, 604, 176
Stetson, P. B. 1987, PASP, 99, 191
Subramaniam, A. 2022, JApA, 43, 80
Subramaniam, A., Sindhu, N., Tandon, S. N., et al. 2016b, ApJL, 833, L27
Subramaniam, A., Tandon, S. N., Hutchings, J., et al. 2016a, Proc. SPIE, 9905, 99051F
Subramanian, S., & Subramaniam, A. 2012, ApJ, 744, 128
Tandon, S. N., Hutchings, J. B., Ghosh, S. K., et al. 2017a, JApA, 38, 28
Tandon, S. N., Postma, J., Joseph, P., et al. 2020, AJ, 159, 158

Tandon, S. N., Subramaniam, A., Girish, V., et al. 2017b, AJ, 154, 128
Tatton, B. L., vanLoon, J. T., Cioni, M.-R. L., et al. 2021, MNRAS, 504, 2983
van der Marel, R. P., & Cioni, M.-R. L. 2001, AJ, 122, 1807
van der Marel, R. P., & Kallivayalil, N. 2014, ApJ, 781, 121
van der Marel, R. P., Kallivayalil, N., & Besla, G. 2008, in IAU Symp. 256, The Magellanic System: Stars, Gas, and Galaxies (Cambridge: Cambridge Univ. Press), 81
van der Marel, R. P., & Sahlmann, J. 2016, ApJL, 832, L23
Vasiliev, E. 2023, MNRAS, 527, 437
Virtanen, P., Gommers, R., Oliphant, T. E., et al. 2020, NatMe, 17, 261
Zaritsky, D., Harris, J., Grebel, E. K., & Thompson, I. B. 2000, ApJL, 534, L53
Zivick, P., Kallivayalil, N., Besla, G., et al. 2019, ApJ, 874, 78
Zivick, P., Kallivayalil, N., van der Marel, R. P., et al. 2018, ApJ, 864, 55